J. Fluid Mech. (2022), *vol*. 932, A49, doi:10.1017/jfm.2021.1032

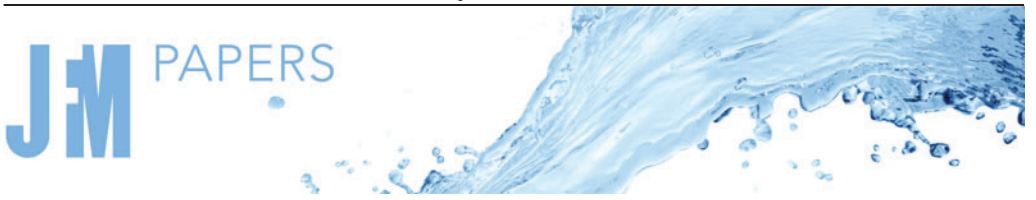

Dripping instability of a two-dimensional liquid film under an inclined plate

Guangzhao Zhou[1] **and Andrea Prosperetti**[1,2,3,†]

[1]Department of Mechanical Engineering, University of Houston, Houston, TX 77204, USA

[2]Faculty of Science and Technology, and J. M. Burgers Center for Fluid Dynamics, University of Twente, 7500 AE Enschede, The Netherlands

[3]Department of Mechanical Engineering, Johns Hopkins University, Baltimore, MD 21218, USA

(Received 20 February 2021; revised 17 September 2021; accepted 15 November 2021)

It is known that the dripping of a liquid film on the underside of a plate can be suppressed by tilting the plate so as to cause a sufficiently strong flow. This paper uses two-dimensional numerical simulations in a closed-flow framework to study several aspects of this phenomenon. It is shown that, in quasi-equilibrium conditions, the onset of dripping is closely associated with the curvature of the wave crests approaching a well-defined maximum value. When dynamic effects become significant, this connection between curvature and dripping weakens, although the critical curvature remains a useful reference point as it is intimately related to the short length scales promoted by the Rayleigh–Taylor instability. In the absence of flow, when the film is on the underside of a horizontal plate, the concept of a limit curvature is relevant only for small liquid volumes close to a critical value. Otherwise, the drops that form have a smaller curvature and a large volume. The paper also illustrates the peculiarly strong dependence of the dripping transition on the initial conditions of the simulations. This feature prevents the development of phase maps dependent only on the governing parameters (Reynolds number, Bond number, etc.) similar to those available for film flow on the upper side of an inclined plate.

Key words: thin films, absolute/convective instability, coating

1. Introduction

After the pioneering work of the Kapitzas (Kapitza 1948; Kapitza & Kapitza 1949), the flow of a liquid film down an inclined plane was recognized as an important topic for scientific and technological reasons, and it has been the object of a vast literature, including monographs (Alekseenko, Nakoryakov & Pokusaev 1994; Chang & Demekhin

† Email address for correspondence: aprosper@central.uh.edu

2002; Kalliadasis *et al.* 2011), review articles (see e.g. Chang 1994; Oron, Davis & Bankoff 1997; Kondic 2003; Weinstein & Ruschak 2004; Craster & Matar 2009) and numerous research papers (see e.g. Rohlfs & Scheid 2015; Rohlfs, Pischke & Scheid 2017; Denner *et al.* 2018; Dietze 2019, and others cited below for recent examples). The majority of this literature concerns the situation in which the film flows on the upper side of the plate with a strong convective instability generating large-amplitude waves when the Reynolds number exceeds an inclination-dependent critical value. Much smaller is the number of studies addressing the converse situation with the film 'hanging' from the underside of the plate. The difference between the two situations is major in that, in the latter one, the Rayleigh–Taylor instability combines and competes with the convective, or Kapitza, instability. When the former mechanism is dominant, drops detach from the film while, when the latter one prevails, stable waves form and propagate along the film. In addition to its scientific interest, this situation is of practical importance in liquid coating, film cooling and some geophysical processes (see e.g. Whitehead 1988; Lister & Kerr 1989; Fermigier *et al.* 1992; Bertagni & Camporeale 2017; Ledda *et al.* 2020, 2021; Lerisson *et al.* 2020).

Early experiments were conducted with layers of very viscous oils on the underside of a nearly horizontal plate (i.e. having an angle of inclination β close to 180°) and focused on pattern formation of falling drops (Fermigier *et al.* 1992; Limat *et al.* 1992). However, dripping can be suppressed in various ways such as plate oscillations (see e.g. Wolf 1969; Talib & Juel 2007; Sterman-Cohen, Bestehorn & Oron 2017), Marangoni flow (see e.g. Deissler & Oron 1992; Sterman-Cohen & Oron 2020), electric fields (Tomlin, Cimpeanu & Papageorgiou 2020), substrate curvature (Trinh *et al.* 2014) and, notably, by a gravity-driven flow along the underside of the plate, as demonstrated by Indeikina, Veretennikov & Chang (1997) and Brun *et al.* (2015), in both of which works no drops were shown to form for sufficient inclinations.

Babchin *et al.* (1983) investigated a related situation in which a layer of lighter fluid rests on a horizontal plate under a large mass of immiscible heavier fluid and considered the saturation of this Rayleigh–Taylor-unstable situation by the motion of the plate in its own plane. Surface tension was identified as the mechanism responsible for this result. Specifically, the flow induced by the plate causes the formation of large-amplitude waves at the interface between the two fluids. Convection shortens the horizontal scale of the waves thus increasing their curvature so much that the surface-tension-induced overpressure prevents additional light liquid from entering them thus stopping their growth. The same mechanism is described by Kalliadasis & Chang (1994) as stabilizing the waves on a liquid-coated vertical fibre and by Indeikina *et al.* (1997) as preventing drop formation in the three-dimensional rivulets covering the underside of a tilted plate. Yiantsios & Higgins (1989) show that, if the plate is stationary, no compression of the wave takes place, the surface deformation does not stop and a drop of lighter fluid may ultimately form and detach unless the effect of surface tension is strong enough. An interesting remark in this paper, also taken up in Kofman *et al.* (2018), connects the shape of the largest stable deformation with that of a pendant drop under a horizontal plate at zero contact angle studied by Pitts (1973). We return to this point later.

While these studies conclusively demonstrate the crucial role of surface tension in preventing drop formation, they leave open the question of the precise conditions and physical mechanism under which this happens. The question is particularly intriguing given the remarkably sharp transition from the dripping to the non-dripping regime as the slope of the plate is increased (see e.g. Kofman *et al.* 2018, and below). Motivated by the work of Duprat *et al.* (2007) on fluid flow down a vertical fibre, the behaviour of

which was interpreted as a transition from an absolute to a convective instability, Brun *et al.* (2015) introduced the hypothesis that a similar transition could be associated with the dripping phenomenon. The idea is that, in the case of an absolute instability, (such as the one prevailing on the underside of a horizontal plate) perturbations remain localized in space leading to dripping while, with a convective instability, growing perturbations move along the inclined plate. The experiments of Brun *et al.* (2015), carried out with a very viscous liquid at negligible Reynolds number, were in rough agreement with this hypothesis. The recent work by Tomlin *et al.* (2020) appeals to the same idea to explain the stabilizing effect of an electric field showing that the absolute–convective transition criterion provides an order-of-magnitude estimate for the electric field strength required to suppress dripping.

The matter was examined theoretically, including inertia, by Scheid, Kofman & Rohlfs (2016) who made use of the two-dimensional reduced model based on the weighted integral boundary layer approach developed by Ruyer-Quil & Manneville (2000). For each value of the Kapitza number, defined below, a maximum inclination angle was identified below which the instability is always convective while it can be of either type above it. The absolute/convective transition is non-monotonic, with the region of absolute Rayleigh–Taylor instability flanked by two regions of convective instability, a small-Reynolds-number one dominated by surface tension and a larger-Reynolds-number one dominated by inertia. The authors pointed out that their results cannot be unequivocally connected to dripping because it could well happen that, if the waves grow sufficiently as they propagate, dripping might still occur downstream of the position where the liquid is injected. For this reason, while they carefully demarcated the absolute/convective transition as a function of the governing parameters, they did not attempt to establish a specific link between dripping and the nature of the instability.

This aspect was examined in a later paper by the same authors and colleagues (Kofman *et al.* 2018) reporting results of two-dimensional numerical simulations in a computational domain of fixed streamwise extent subject to periodicity conditions, the so-called ‘closed-flow’ paradigm that we also adopt. This set-up permitted them to study whether a wave continued to grow eventually leading to drop detachment and, in this way, it permitted them to address the dripping/non-dripping ambiguity associated with a convective instability. They found that the dripping/non-dripping transition was not well correlated with a change of the nature of the instability but, rather, with the existence of inclination-dependent mechanisms capable of saturating the growth of the wave. The necessarily nonlinear nature of these mechanisms further weakens the absolute/convective hypothesis which can only be studied in the linear regime. Another important feature noted in this study, as well as some earlier ones (Yiantsios & Higgins 1989; Rohlfs *et al.* 2017), is the strong influence of initial conditions on the dripping transition. This important issue is examined in § 7 below.

From this summary it may be concluded that no clarity exists as to the dripping/non-dripping transition of a liquid film flowing on the underside of an inclined plate. In this paper we address this problem adopting the same closed-flow set-up of Kofman *et al.* (2018), Sterman-Cohen *et al.* (2017), Sterman-Cohen & Oron (2020) and Rohlfs *et al.* (2017) (the last authors also used the open flow set-up). We study the two-dimensional version of the problem in spite of its somewhat idealized nature *vis-à-vis* the actual physical situation. Indeed, it is well-known that the Rayleigh–Taylor instability acts on the film not only in the vertical direction, but also in the spanwise direction, leading to the formation of rivulets from which, in appropriate conditions, droplets can detach. This aspect has been studied both experimentally and theoretically in several papers (Indeikina *et al.* 1997; Lin, Kondic & Filippov 2012; Rietz *et al.* 2017; Charogiannis

et al. 2018; Ledda *et al.* 2020, 2021; Lerisson *et al.* 2020). However, the fact that many of the theoretical studies mentioned before deal with the two-dimensional problem (e.g. Lin & Kondic 2010; Rohlfs & Scheid 2015; Rohlfs *et al.* 2017; Sterman-Cohen *et al.* 2017; Denner *et al.* 2018; Kofman *et al.* 2018; Dietze 2019; Sterman-Cohen & Oron 2020, and many others) is a proof of the continuing relevance and usefulness of this idealization. In the first place, the three-dimensional structures take some distance to develop downstream of the inlet and are preceded by two-dimensional waves (see e.g. Rietz *et al.* 2017), unless they are artificially generated directly at the inlet as, e.g. in Ledda *et al.* (2020) and Lerisson *et al.* (2020). Secondly, the large literature on this general topic is an eloquent demonstration of the subtlety and complexity of the physical processes involved. A frontal attack on the complete problem may not be the most efficient way to unravel them not only for intellectual, but also for practical reasons due to the need for extensive computation and the considerably longer time required by three-dimensional vs two-dimensional simulations. Progress on the simpler two-dimensional problem would be faster and may be expected to provide useful keys for the complete understanding of the more relevant three-dimensional one. Finally, the two-dimensional problem is of interest in itself as a test bed for the development of long-wave asymptotic methods (see e.g. Chang 1994; Oron *et al.* 1997; Ruyer-Quil & Manneville 2000; Kalliadasis *et al.* 2011) and as a relatively tractable example of an infinite-dimensional dynamical system (see e.g. Pumir, Manneville & Pomeau 1983; Chang & Demekhin 2002; Lin & Kondic 2010).

After a brief outline of the numerical method (§ 2), the paper starts by describing simulations of waves on the underside of a plate the inclination of which is very slowly reduced (§ 3). In this situation, dripping happens under quasi-equilibrium conditions and is characterized by the curvature at the wave crest approaching a limit value (§ 4). When dynamic effects gain importance, the connection between curvature and dripping weakens, but can still be recognized (§ 5). The case of dripping from a horizontal plate is useful in understanding the dripping from plates which are only slightly inclined and as a paradigm for situations far from critical conditions (§ 6). The last topic is the importance of initial conditions which is illustrated with several examples (§ 7).

2. Numerical simulations

We carry out two-dimensional numerical simulations in the so-called closed-flow framework in which the Navier–Stokes equations are solved in a computational domain of length L along the flow direction x and the flow fields satisfy periodicity boundary conditions at $x = 0$ and $x = L$; y is the coordinate normal to the plate. The no-slip condition is applied at the plate surface located at $y = 0$.

The calculations have been performed with the open-source code Basilisk (http://basilisk.fr), an improved version of the code Gerris used by Kofman *et al.* (2018). The code adopts a second-order time- and space-adaptive finite volume methodology based on a projection method with a quadtree discretization (Scardovelli & Zaleski 1999; Popinet 2009). A conservative, non-diffusive, geometric volume-of-fluid method is used to simulate a gas–liquid two-phase flow. The interface between the phases is described by a volume fraction field which is governed by an advection equation. An improved version of the continuum surface force method (Brackbill, Kothe & Zemach 1992; François *et al.* 2006) is used to account for surface-tension effects. We have assigned a density and viscosity 1000 times smaller than those of the liquid to the gas phase, thus approximating a situation in which the gas has negligible dynamical effects on the liquid. By varying these ratios we have confirmed that, with the choices made, the gas phase indeed has a negligible influence on the calculations. We have allowed a maximum grid refinement down to $2^{-11}L$

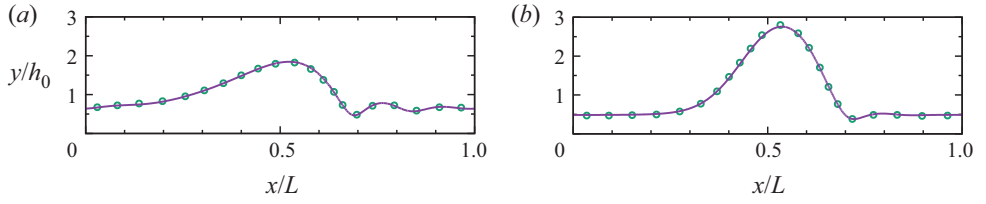

Figure 1. Comparison of the present simulations (continuous lines) with the published results in figures 2(*a*) and 2(*b*) of Kofman *et al.* (2018).

finding good numerical convergence. A comparison of the results of our simulations (solid lines) with the Gerris data taken from the published figures 2(*a*) and 2(*b*) of Kofman *et al.* (2018) (circles), shown in figure 1, supports the reliability of our simulations.

The cases simulated can be characterized in terms of four dimensionless parameters. We choose V/h_0^2, the volume of liquid V in the computational domain (per unit spanwise length) non-dimensionalized by the mean film thickness h_0, the inclination angle β (defined so that the plate is vertical for $\beta = \pi/2$ and horizontal with the film on its underside for $\beta = \pi$) and the Reynolds and Bond numbers. It has been customary in the literature on film flow on the upper side of inclined plates to incorporate the inclination angle into the definition of these numbers

$$Re = \frac{h_0^3 g \sin\beta}{3\nu^2}, \quad Bo = \frac{\rho h_0^2 g \sin\beta}{\sigma}, \tag{2.1a,b}$$

with g the acceleration of gravity, ν and ρ the liquid kinematic viscosity and density and σ the surface-tension coefficient. The same definitions are used by several authors also for film flow on the underside of inclined plates. However, when the effect of gravity normal to the plate becomes critical, as in this latter configuration, the effect of the angle cannot be completely captured by these definitions and this is the reason we consider the angle itself as a separate fourth parameter. Following other researchers (see e.g. Rohlfs *et al.* 2017; Charogiannis *et al.* 2018), in order to characterize the simulations we use the so-called vertical version of the Reynolds and Bond numbers, $Re_\perp$ and $Bo_\perp$, defined as above by setting $\sin\beta = 1$. Another dimensionless quantity encountered in the literature is the Kapitza number Ka which can be expressed in terms of our primary dimensionless quantities as $Ka = (3Re)^{2/3}/Bo$, and $Ka_\perp = (3Re_\perp)^{2/3}/Bo_\perp$. The capillary length $\ell_c = \sqrt{\sigma/\rho g}$, not adjusted for the plate inclination, is related to the vertical Bond number by $h_0/\ell_c = \sqrt{Bo_\perp}$.

3. The quasi-equilibrium case

We carried out simulations with the slope of the plate very slowly reduced (i.e. the angle β slowly increased towards 180°) starting from a computed steady non-dripping Kapitza wave. The rate of increase of the angle was 0.05° per dimensionless time unit $\sqrt{g/h_0}\,t = 1$ and was therefore so slow that the results can be considered as essentially progressing through a sequence of steady states until dripping sets in. By the way these simulations have been conducted, the gradual approach to the onset of dripping changes the liquid momentum of the growing wave at a very slow rate. The dripping that eventually sets in when the plate inclination is small enough is therefore little influenced by dynamic effects normal to the plate and essentially occurs when surface tension can no longer support the wave crest against gravity. For this reason, the dripping thresholds that we determine in this way can be considered upper limits. Indeed, we will show later examples in which,

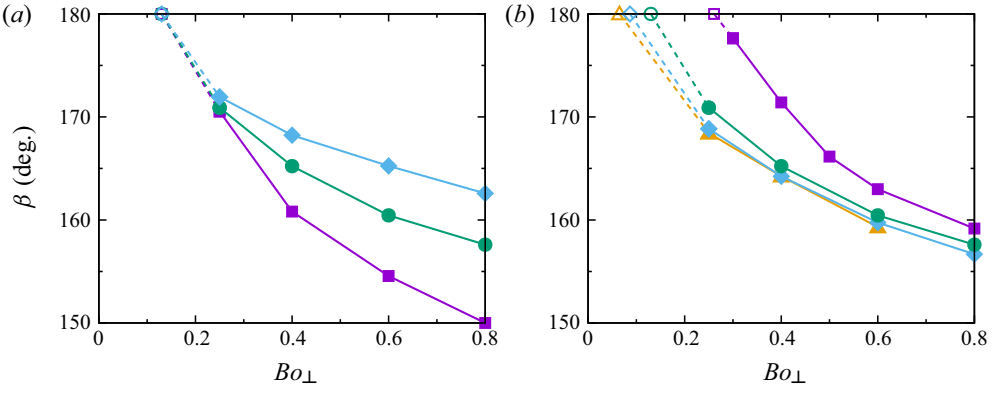

Figure 2. (*a*) Dripping threshold vs the perpendicular Bond number $Bo_\perp$ for $V/h_0^2 = 40$ and, in descending order, $Re_\perp = 100$, 50 and 20. (*b*) Dripping threshold vs $Bo_\perp$ for $Re_\perp = 50$ and, in descending order, $V/h_0^2 = 20$, 40, 60 and 80.

due to the rapid growth of the Rayleigh–Taylor instability, dripping takes place at smaller angles for the same values of $Re_\perp$, $Bo_\perp$ and V/h_0^2.

Figures 2(*a*) and 2(*b*) show some results for the dripping threshold as a function of the problem parameters $Re_\perp$, $Bo_\perp$ and V/h_0^2. The limit points for $\beta = 180^\circ$ shown in the figures correspond to the minimum liquid volume necessary for dripping from a horizontal plate and are explained in § 6. Figure 2(*a*) shows that the wave is increasingly stable as the Reynolds number $Re_\perp$ is increased from 20 (squares, purple) to 50 (circles, green) to 100 (diamonds, blue), so that the angle corresponding to the dripping threshold increases and the plate inclination decreases. As the Bond number decreases, the effect of surface tension increases, a smaller flow rate is sufficient to stabilize the wave and the dripping angle increases.

Figure 2(*b*) shows that increasing the total liquid volume has a destabilizing effect, which causes the dripping angle to decrease and the plate inclination necessary for stability to increase. The primary reason is that, with more liquid available, the wave crest can grow fed by liquid that can flow into it remaining relatively far from the wall and, therefore, relatively unimpeded by the viscous shear caused by the no-slip condition. A heavier wave crest requires a stronger surface-tension effect to be supported against gravity and, therefore, a decreasing $Bo_\perp$ has a stabilizing effect. While increasing the liquid volume from 20 to 40 has a strong effect, further increases have a progressively weaker influence because for $V/h_0^2 = 40$ there is already enough liquid able to flow into the wave crest. Some of these considerations are amplified and better justified later in § 6.

Figure 3 shows three examples of the waveform at the instant at which $\beta = 160^\circ$ with $Bo_\perp = 0.4$, $V/h_0^2 = 40$ and $Re_\perp = 20$, 50 and 100, all of which are stable cases. It is interesting to note the thickening of the wave tail as the Reynolds number is increased. This feature is reminiscent of the phenomenon encountered when a plate is pulled out of a liquid bath, in which process the thickness of the film left on the plate increases with the withdrawal velocity for a fixed Kapitza number (see e.g. Orsini & Tricoli 2017). By conservation of volume, the thickening of the wave tail decreases the wave amplitude, the volume of liquid in the crest and the crest curvature. We will return in § 5 on the importance of these factors in stabilizing the wave.

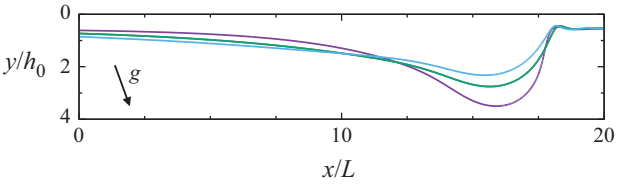

Figure 3. Three examples of the stable (non-dripping) wave shapes for $\beta = 160^\circ$ for $Re_\perp = 20$ (purple), 50 (green) and 100 (blue) with $Bo_\perp = 0.4$ and $V/h_0^2 = 40$.

4. Curvature of the wave crest

An interesting feature of the simulations just described is illustrated in figure 4 for a few cases ($Re_\perp$ = 50 and 100, $Bo_\perp$ = 0.4, 0.6 and 0.8, and V/h_0^2 = 20, 40 and 80) but the same feature is also present in all the other cases used to generate the dripping thresholds of figure 2. Panel (*a*) of the figure shows the dimensionless growth rate $(\mathrm{d}h_w/\mathrm{d}t)/\sqrt{gh_0}$ of the amplitude h_w of the wave under the plate while (*b*) shows κ_w, the curvature at the wave crest, non-dimensionalized by the capillary length ℓ_c, both as functions of the dimensionless time $\sqrt{g/h_0}t$. In all cases, the growth rate of the waves starts to increase very rapidly once the dimensionless maximum curvature approaches a particular value $\kappa_{cr} \simeq 1.187/\ell_c$. We have found that, if the angle of inclination of the plate is kept constant just before this value is reached, the wave remains steady while, if it is stopped just above, the wave amplitude keeps increasing until a drop forms and detaches. This fact suggests that κ_{cr} corresponds to or, at least, is correlated with, the dripping threshold in the condition of these simulations.

After reaching κ_{cr}, the tip curvature continues to increase rapidly approaching a maximum value close to $\kappa_\parallel = \sqrt{2}/\ell_c$ and then, equally rapidly, it starts to decrease until a drop forms and detaches at approximately the time the curvature has returned to κ_{cr}. The volumes (areas) of these drops are found to be very close to each other and approximately given by $4.6\ell_c^2$. A similar sequence can be observed in figure 10(*b*) of Yiantsios & Higgins (1989), in which the curvature of the drop tip is seen to increase up to the point at which the drop develops inflection points with vertical tangents, after which it starts to decrease.

The shapes of the wave as the angle of inclination gradually increases (i.e. the plate slope decreases) are shown in figure 5 for the case $Re_\perp = 50$, $Bo_\perp = 0.6$ and $V/h_0^2 = 40$; those for the other cases go through a similar progression. As the slope decreases the amplitude of the wave increases. The last profile shown is taken at the point at which the curvature reaches its maximum just before the base of the drop starts to shrink prior to detaching.

In order to rationalize these results we refer to the observation of Pitts (1973) who studied the static equilibrium of a given amount of liquid attached to the underside of a horizontal plate with a prescribed contact angle. He calculated the volume (per unit spanwise length) of liquid which remains in equilibrium under the action of gravity and surface tension as a function of h_{drop}, the elongation of the drop under the plate and, for each volume, found two values of h_{drop}, the larger one corresponding to unstable and the smaller one to stable equilibrium. For a zero contact angle, the two branches come together at a maximum volume $V_{cr} \simeq 5.211\ell_c^2$, at which point the height of the drop is $h_{cr} \simeq 2.374\,\ell_c$ with the tip curvature $\kappa_{cr} \simeq 1.187/\ell_c$. No equilibrium solution exists for liquid volumes greater than V_{cr}.

While Pitts used an energy argument, his results on the equilibrium drop shape are readily obtained from the relation which expresses the balance of surface tension and

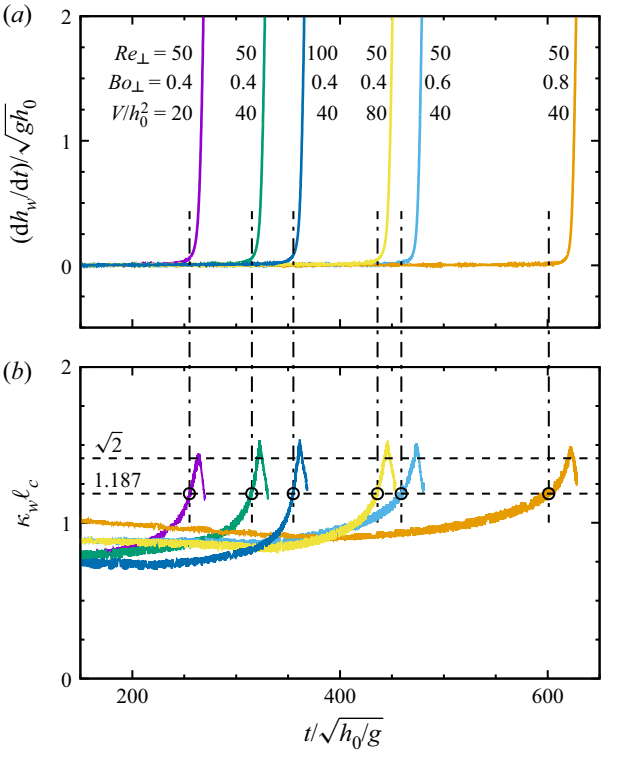

Figure 4. (*a*) Growth rate of the wave amplitude. (*b*) Curvature of the wave crest vs time as the slope of the plate is slowly reduced. The plate inclination angles at the instants marked by the vertical dashed lines are, from left to right, 171.4°, 165.2°, 168.2°, 164.3°, 160.5° and 157.6°.

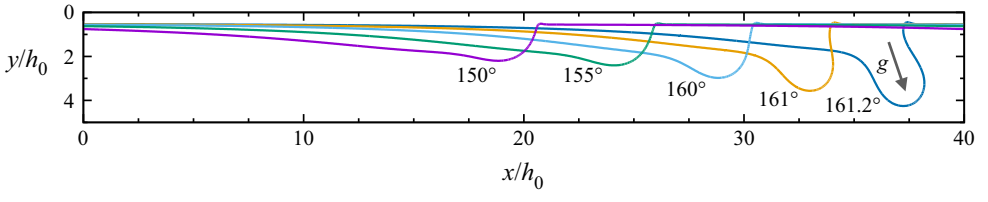

Figure 5. Wave shapes at different plate inclination angles for the case $Re = 50$, $Bo = 0.6$ and $V/h_0^2 = 40$ of the previous figure; the dimensionless times are $\sqrt{g/h_0}\,t = 250$, 350, 450, 470 and 474.

gravity for a pendant drop under a horizontal plate, namely (see Appendix A)

$$\sigma\kappa(z) = \sigma\kappa_0 - \rho g z. \tag{4.1}$$

Here, z is the vertical distance from the tip of the pendant drop to the generic point on the drop surface, $\kappa(z)$ the surface curvature at that point and κ_0 the curvature at the drop tip. Figure 6(*a*) shows the dimensionless pendant drop volume (per unit spanwise length) V_{drop}/ℓ_c^2 vs the dimensionless elongation h_{drop}/ℓ_c for zero contact angle and agrees with figure 3 of Pitts (see also figure 12 of Yiantsios & Higgins 1989).

Figure 4 implies that the balance argument of Pitts is relevant not only for the equilibrium drop under a horizontal plate, but also for the crest of a quasi-steady Kapitza wave. Kofman *et al.* (2018) also referred to Pitts' result using directly the limit volume

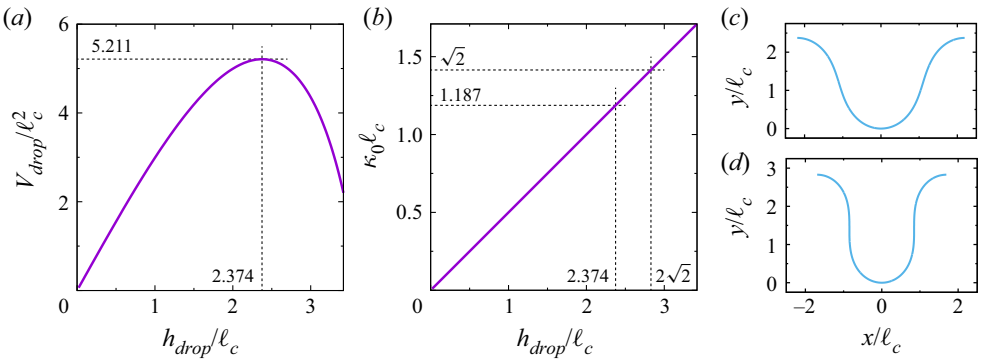

Figure 6. (*a*) Volume of a static pendant drop under a horizontal plate vs drop elongation under the plate for zero contact angle; the dashed lines mark the stability limit. (*b*) Curvature vs drop elongation. (*c*) Drop shape when $\ell_c\kappa_{cr} = 1.187$. (*d*) Drop shape when $\ell_c\kappa_{\parallel} = \sqrt{2}$.

$V_{cr} \simeq 5.211\ell_c^2$, with ℓ_c adjusted for the inclination of the plate, as an indicator of the dripping threshold. Possibly because of fluid momentum effects in their waves, and even though they subtracted the volume of the liquid substrate (the definition of which may be somewhat uncertain, due to the fact that a significant amount of liquid accumulates in the tail of the wave above the substrate) their results were only moderately successful ranging from $\sim 4\ell_c^2$ to $\sim 8\ell_c^2$ about Pitts' value $V_{cr} = 5.211\ell_c^2$. Some considerations on the scaling suggested by Kofman *et al.* (2018) can be found in Appendix B.

The way in which we propose to use Pitts' result is less direct but not dependent on the ambiguity associated with the drop volume or, because of the way the results of figure 4 were generated, on momentum effects. According to figure 6(*a*), Pitts' drop volume is in a one-to-one correspondence with the drop elongation. By establishing a connection between the drop elongation h_{drop} and the tip curvature we can then relate the limit volume V_{cr} to the curvature of the drop tip κ_{cr}. For this purpose we note that it is a simple consequence of (4.1) that, for a zero contact angle, the curvature at the tip of the drop satisfies the relation

$$\kappa_0 = \frac{h_{drop}}{2\ell_c^2}. \tag{4.2}$$

This result, together with other considerations related to (4.1), is proven in Appendix A. The relation (4.2) permits us to cast the drop elongation $h_{drop} = h_{cr}$ corresponding to the limit volume V_{cr} into a critical value for the curvature at the drop tip, $\ell_c\kappa_{cr} \simeq 1.187$ marked in figure 4. The correspondence between the tip curvature and the drop elongation shows that the former is closely related to the ability of surface and potential energies to balance each other. The drop shape corresponding to the tip curvature κ_{cr} is shown in figure 6(*c*); this shape is the same as that shown in figure 12 of Yiantsios & Higgins. The significance of the conditions under which the tip curvature reaches κ_{cr} is that, past this point, the release of potential energy associated with a further increase of the drop elongation can no longer be balanced by a corresponding increase of surface energy. Conservation of energy requires the appearance of another pathway to channel the excess potential energy released, and this is the kinetic energy of the forming and detaching drop, with the attendant viscous dissipation.

There is another pendant drop configuration that is worthy of specific attention. As the elongation of a pendant drop increases, its width near the base narrows and, at some point, a shape develops characterized by vertical tangents at the inflection points as

shown in figure 6(*d*). The special importance of this configuration resides in the fact that, when it occurs, the surface tension force acts vertically and is therefore most effective in counteracting gravity. As shown in Appendix A, the corresponding crest curvature equals $\kappa_\parallel = \sqrt{2}/\ell_c$ and is also marked in figure 4. In equilibrium conditions, the pressure along the line joining the two inflection points is evidently the constant external pressure and, if the volume of liquid under this line is V_M, equilibrium requires that $\rho g V_M = 2\sigma$ or $V_M = 2\ell_c^2$. Any increase beyond V_M of the amount of liquid in the region below the line cannot be sustained by surface tension and a drop must eventually detach. The total liquid volume corresponding to the curvature $\kappa_\parallel$ is calculated in Appendix A for zero contact angle and it is found to be $V_\parallel \simeq 4.793\ell_c^2$. It is therefore smaller than that corresponding to κ_{cr}, but the result $\kappa_\parallel = \sqrt{2}/\ell_c$ can be derived without reference to the total liquid volume, just focusing on the portion of the pendant drop between the tip and the points of vertical tangency. Thus, unlike κ_{cr}, $\kappa_\parallel$ is independent of the total amount of liquid under the plate and characterizes the largest liquid volume that can be sustained by surface tension under equilibrium conditions. This feature confers to this value of the curvature and the associated volume V_M a special importance as we will see.

It is interesting to observe that, as can be seen in the examples of figure 7, the actual shape of the wave crest closely approximates the shapes shown in figures 6(*c*) and 6(*d*) at the instants when its curvature reaches κ_{cr} and $\kappa_\parallel$. In the figure the two drop shapes of figures 6(*c*) and 6(*d*) are rotated and superposed on the wave crest at these times without any further adjustment. The axis of the drop shapes are nearly coincident with the direction of gravity, also shown by the arrows in the figure, with the slight misalignment a consequence of the wave momentum. This alignment justifies the use of ℓ_c as defined before without any adjustment for the plate inclination. The match between the drop and wave shapes is very nearly perfect for panels (*b*) and (*d*), for which $\kappa_w = \kappa_\parallel$. These results imply that the balance between surface and gravitational energies, that determines the dripping stability of a static drop under a horizontal plate, also determines, to a good approximation, the stability of quasi-equilibrium Kapitza waves. This connection between tip curvature and drop formation suggests that processes tending to stretch the base of the crest, thus preventing its curvature from approaching the critical value, will have a stabilizing effect against dripping. This appears to be a major mechanism by which flow stabilizes the wave as will be further argued below.

This mechanism is inherently nonlinear and is therefore incompatible with an explanation based on the transition from absolute to convective instability of Brun *et al.* (2015) and others. The mechanism proposed by Babchin *et al.* (1983), who saw the convective steepening of the wave as stabilizing the Rayleigh–Taylor instability by increasing, rather than decreasing, the curvature of the wave crest, is only superficially incompatible with our proposal. What happens is that, indeed, the increasing curvature initially opposes the growth of the Rayleigh–Taylor instability but, if it were to be allowed to continue, it would shrink the base of the crest so much that a drop would form and detach. To stabilize the wave, therefore, it is necessary that the growth of the crest curvature be arrested before it becomes critical.

5. Normal momentum

It is evident from the wave shapes such as those shown in figure 5 that dripping may be influenced by the entire wave, but is ultimately a phenomenon localized at the wave crest. In the quasi-equilibrium situations of the previous section, the curvature of the crest is significant because it quantifies the amount of liquid in the crest and the crest length scale,

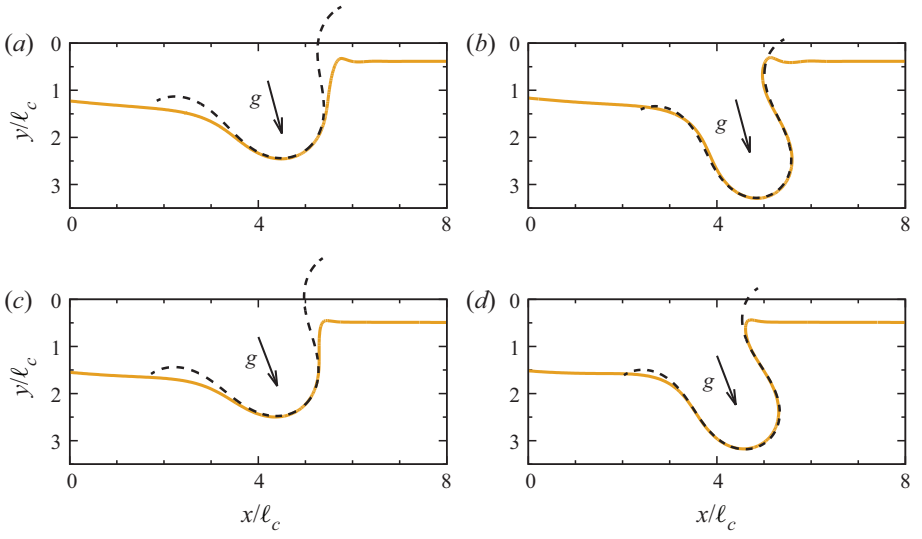

Figure 7. Drop shapes of figures 6(*c*) and 6(*d*) rotated and superimposed on the wave profiles at the moment the corresponding curvatures are reached for $Re = 50$; (*a*,*b*) $Bo = 0.4$, $V/h_0^2 = 80$, $\beta \simeq 165°$; (*c*,*d*) $Bo = 0.8$, $V/h_0^2 = 40$, $\beta \simeq 150°$. The arrows indicate the direction of gravity.

which determine the propensity to instability thanks to the fact that the dominant forces at play are surface tension and gravity. The very fact that results obtained for the curvature of an equilibrium drop match well the results of quasi-equilibrium dynamical simulations gives a clear indication of the small importance of inertia and flow in the phenomena simulated in §§ 3 and 4. Of course there is recirculation in the wave (see e.g. Reck & Aksel 2015; Rohlfs & Scheid 2015; Rohlfs *et al.* 2017), but the associated flow is so weak that its effect is not noticeable in the results of the previous two sections. As the flow is allowed to develop naturally rather than being guided, as it were, through a succession of quasi-equilibrium states, other channels for the potential energy released by the falling of the liquid near the crest become available beyond surface energy, namely kinetic energy and viscous dissipation. Furthermore, localized disturbances can also affect the wave and, in particular, its crest. It may well be expected, therefore, that at the stability limit the direct relation between curvature and stability valid for quasi-static equilibrium will be affected when dynamic effects become significant.

Figure 8 shows some typical examples of how the momentum of the developing wave normal to the plate affects the curvature of the wave crest when the calculation is started from a sinusoidal perturbation

$$\frac{h(x, t = 0)}{h_0} = 1 + A \sin \frac{2\pi x}{L}, \tag{5.1}$$

with an initial amplitude $A = 0.2$; here, $Re_\perp = 50$, $Bo_\perp = 0.6$ and $V/h_0^2 = 40$. With $h_0 = 1\,\mathrm{mm}$ and typical properties of a silicone oil, $\sigma = 21\,\mathrm{mN\,m^{-1}}$, $\rho = 971\,\mathrm{kg\,m^{-3}}$, $\nu = 8 \times 10^{-6}\,\mathrm{m^2\,s^{-1}}$, we find $Bo_\perp = 0.45$ and $Re_\perp \simeq 51$. The parameter choice can therefore be considered as representative of real situations. In the figure, the various lines correspond to different angles of inclination, kept fixed for each simulation. A prominent feature of these results is the evidence of finite-amplitude oscillations of the crest curvature which highlight the fundamental difference with the earlier simulations of figure 4. A closer inspection shows the presence of a smaller and faster oscillations super-imposed

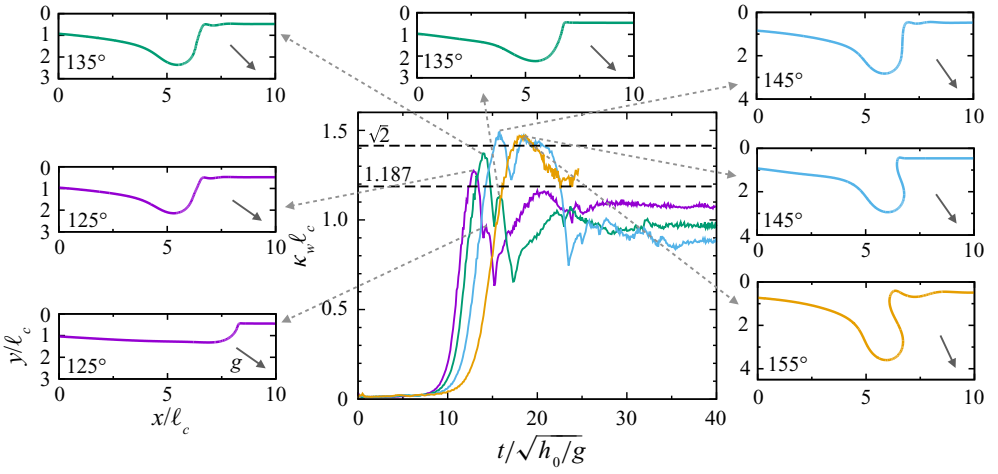

Figure 8. Curvature vs time as waves evolve for different fixed inclination angles with $Re_\perp = 50$, $Bo_\perp = 0.6$, $V/h_0^2 = 40$. The wave shapes are taken at the instant marked in the figure.

on a slower one. The computations show that the faster oscillation is caused by the absorption of a small disturbance at the front of the wave associated with the initial rapid phase of growth. For each image pair in figure 8 this disturbance is visible in the frame corresponding to the first peak and is shown more clearly for one example in movie 1 of the supplementary material associated with this paper available at https://doi.org/10.1017/jfm.2021.1032. Similar oscillations can also be seen in the supplemental material of Zhou & Prosperetti (2020). The slower oscillations reflect the oscillations of the entire wave and are reminiscent of those mentioned in Babchin *et al.* (1983) who write 'As a result of the combined effect of these three factors – destabilizing gravity, flow-induced scale contractions, and stabilizing surface tension – finite-amplitude oscillations set in'.

A sequence showing wave profiles over the course of the slow oscillation is shown in figure 9 for the case $\beta = 145°$ of figure 8. The figure shows successive images of the wave separated by equal time intervals $\sqrt{g/h_0}\,\Delta t = 2$ starting from $\sqrt{g/h_0}\,t = 13$. The faster, small-amplitude oscillation is revealed by a careful look at the waveforms, but the slower, larger one is quite clear. As the oscillation amplitude decreases, liquid is pushed back toward the plate and tends to flow forward (possibly because of the low surface-tension-induced pressure at the foot of the wave), thus increasing the apparent speed of the wave front. In this process the tail grows 'stretching' the back of the wave, increasing the length scale of the crest and, with it, decreasing the crest curvature.

A portion of the waveform at the maximum points of the curvature oscillations is shown in the small images surrounding the main panel of figure 8. Here the crest shape is not determined solely by a surface-tension/gravity equilibrium, but is significantly influenced by dynamic effects. This can be seen, for example, from the difference between the first crest shape for $\beta = 125°$ (middle inset on the left) and the shape shown in figure 6(*c*) in spite of the fact that, in both cases, the tip curvature is close to κ_{cr}. A careful inspection of the insets for $\beta = 135°$, $145°$ and $155°$ shows that the wave tail thickens as the inclination increases; we will see later in figure 14 that, conversely, the tail is very strongly reduced by further decreases of the plate inclination. The same thickening is shown in figure 3 where it is produced by the increase of the Reynolds number. For the same substrate thickness, a thicker tail takes liquid away from the crest thus limiting the amount of liquid available

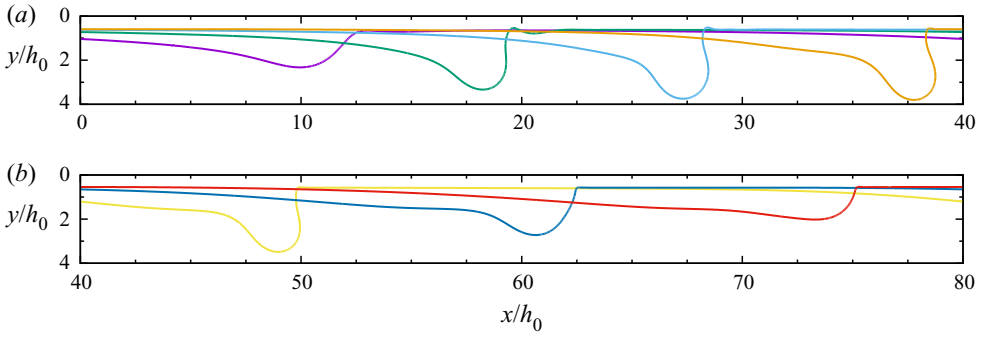

Figure 9. A sequence of wave shapes for the case $\beta = 145^\circ$ of figure 8; the images are separated by equal time intervals $\sqrt{g/h_0}\,\Delta t = 2$ starting from $\sqrt{g/h_0}\,t = 13$. Note how the growth of the tail ultimately 'stretches' the wave crest and diminishes its curvature.

to form a drop and 'stretches' the wave, thus increasing the length scale of the crest. Both factors increase with the inclination of the plate and exert a stabilizing effect on the wave.

In all cases of figure 8 excepting the last one for 155°, the crest curvature ultimately decays without drop formation. When the curvature exceeds $\kappa_\parallel = \sqrt{2}/\ell_c$ the wave shape closely resembles the one shown in figure 6(*d*), both for the stable case $\beta = 145^\circ$ and the unstable case $\beta = 155^\circ$. In the former, the wave shape is close to that of figure 6(*d*), but the tangents at the inflection points of the wave shape do not quite become parallel to gravity and no drop forms. For the unstable $\beta = 155^\circ$ case, however, the wave shape has evidently just passed the point of vertical tangency and, indeed, the wave becomes unstable and a drop detaches. These results suggest that $\kappa_\parallel$ maintains its correlation with the maximum liquid volume that can be supported by surface tension even in the presence of moderate dynamic effects. We have encountered stable waves with maximum curvatures temporarily larger than $\kappa_\parallel$ only when the wave was excited by short-wavelength disturbances, stronger than the ones giving rise to the oscillations visible in figure 8 mentioned before. In these cases, however, the large curvature was not associated with a sufficient liquid volume to overcome surface tension and, in any case, the large curvature did not last long enough to allow for the formation and detachment of a drop. Generalizing, it might be said that, in most cases, the shortest length scales that can arise are those generated by the Rayleigh–Taylor instability for which the crest curvature is a good indicator.

It may also be noted that here we find dripping for $\beta = 155^\circ$ while, for the same parameter values, in the quasi-equilibrium case of figure 4 dripping did not occur until the inclination reached an angle $\beta = 160.5^\circ$. The decrease of the dripping angle that we encounter here arises from the fact that, evolving from the initial condition, the wave is off-equilibrium. As the liquid gets re-distributed and the velocity field develops, a sufficient and sufficiently persistent accumulation of liquid in the wave crest can occur to overcome the restraining power of surface tension. Through this process, dynamic effects can render unstable a situation that would be stable in quasi-equilibrium conditions. These considerations support the interpretation of the conditions of figure 4 as providing an upper limit for dripping. We will see further examples when we explore the effect of initial conditions in § 7.

6. Horizontal and nearly horizontal plate

Up to this point we have considered plate inclination angles lower than, or just above, the critical angle for dripping. In preparation for the study of phenomena occurring farther

from criticality, it is useful to consider the largest possible angle, i.e. a horizontal plate with $\beta = 180^\circ$. As we will see, away from criticality the evolution of the system can be quite different from the one outlined in the previous sections and conclusions based on the quasi-equilibrium picture become less and less applicable. Some qualitative features of the results that we find in this case will also be encountered in the next section where, in the study of the effect of initial conditions, we encounter situations far from criticality because of conditions other than the angle of inclination of the plate. As will be noted in the next section, this is a consequence of the large (actually, infinite) dimensionality of the parameter space of the problem at hand which can in no way be reduced to considerations based on linear theory.

A fundamental study of the Rayleigh–Taylor instability with a horizontal plate was conducted by Yiantsios & Higgins (1989) who considered two superposed fluids in the Stokes flow limit. The same configuration was studied by others (see e.g. Whitehead 1988; Lister & Kerr 1989), but we refer to Yantsios & Higgins' study as, although their configuration is different from ours, many of their results are relevant. For example, these authors demonstrated the strong effect of initial conditions, a feature that we have already encountered and which we will illustrate further in the next section. They pointed out the limitations of predictions based on the (linear) fastest growing wavelength which may or may not dominate the final outcome of the instability and, in addition, they demonstrated the importance of the total liquid volume. Another somewhat distantly related work is that of Elgowainy & Ashgriz (1997) who studied an unsupported liquid layer subjected to a pressure difference on its two sides. The absence of a supporting plate makes the results of this study of limited use for our intents, but the growth of the so-called Rayleigh–Taylor spikes has some similarities with the example shown later in figure 11.

We focus on the dependence of the crest curvature on the total liquid volume in the computational domain. Of particular interest is the maximum curvature which is reached just before a drop starts to form. We fix L/ℓ_c, the domain length normalized by the capillary length, and study the effect of varying the normalized film thickness h_0/ℓ_c. The initial interface configuration is prescribed as before in (5.1) with $A = 0.1$. Several examples of the time dependence of the drop tip curvature are shown in figure 10 for $L/\ell_c = 10$ and different normalized liquid volumes $V/V_{cr} = Lh_0/V_{cr}$. In the present situation in which there is no travelling wave, a suitable dimensionless quantity to characterize the effect of viscosity is the Ohnesorge number

$$Oh = \frac{\mu}{\sqrt{\sigma\rho h_0}} = Ka_\perp^{-3/4} Bo_\perp^{-1/4}, \tag{6.1}$$

which is a measure of the viscous damping rate to the frequency of capillary waves. For the examples of figure 10 Oh ranges, from left to right, from 0.050 to 0.120. In all cases, at first the curvature increases with time. As the initial wave crest gradually forms into a pendant drop, the curvature attains a maximum value soon after the free surface has developed two inflection points with vertical tangents. The curvature then briefly relaxes as the drop forms and starts to fall away from the plate reaching the bottom of the computational domain. The simulations are stopped at this point. We have found very similar results for $L/\ell_c = 8$, 12 and 15. The Ohnesorge number controls the speed of the process but also, not coincidentally, the maximum curvature, which is seen to increase as the process is slowed down, which causes an increase of the importance of viscosity and a concomitant decrease of dynamic effects.

Smaller values of Oh facilitate the formation of drops that are larger than the volumes V_{cr} and $V_\parallel$ of figures 6(*c*) and 6(*d*) and have a curvature smaller than κ_{cr} and $\kappa_\parallel$. An example is shown in figure 11 which compares the pendant drop shape for $Oh = 0.05$ and

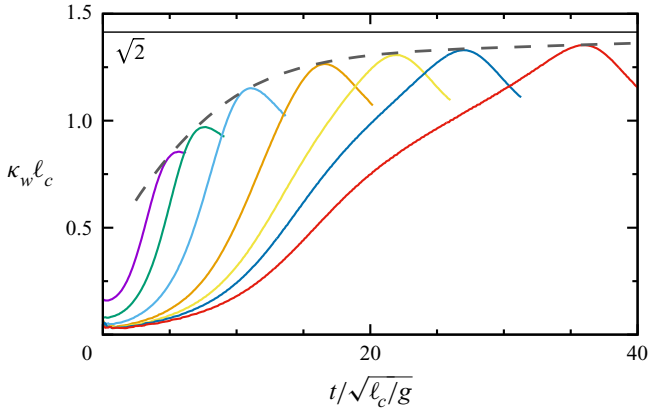

Figure 10. Time dependence of the curvature at the tip of a pendant drop under a horizontal plate for $L/\ell_c = 10$. From left to right, the curves are for Ohnesorge numbers, defined in (6.1), equal to 0.050, 0.071, 0.091, 0.105, 0.112, 0.115 and 0.120. The computations show that the maximum curvature is reached just after the free surface develops two inflection points with vertical tangents and then relaxes as the base of the drop shrinks leading to detachment. The dashed line is a guide to the eye.

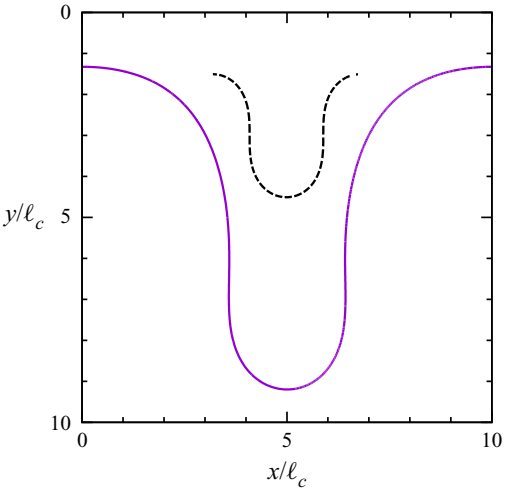

Figure 11. An example of the shape of a pendant drop under a horizontal plate at the moment at which two inflection points with vertical tangents appear; here, $Oh = 0.05$ and $L/\ell_c = 10$. The dashed line permits a comparison with the equilibrium shape of Pitts shown in figure 6(*d*) and drawn to the same scale.

$L/\ell_c = 10$, at the moment inflection points with vertical tangents appear, with the drop of figure 6(*d*) drawn at the same scale. In this case, the volume of the drop that ultimately detaches is more than three times as large as the volume of the drops that detach when the waves of figure 4 become unstable. A similar finding was reported by Abdelall *et al.* (2006) who experimented with drop detachment from the underside of a porous plate. The reason is that, unlike the drops found following Pitts' analysis, the drop shapes that develop in these conditions are not equilibrium solutions of the gravity–surface-tension balance relation (4.1). An intuitive explanation of these results may be given noting that a liquid flow accelerating in the direction of gravity is, in a very rough sense, equivalent to a reduced gravity since, if the liquid was in a free fall, the apparent gravity would

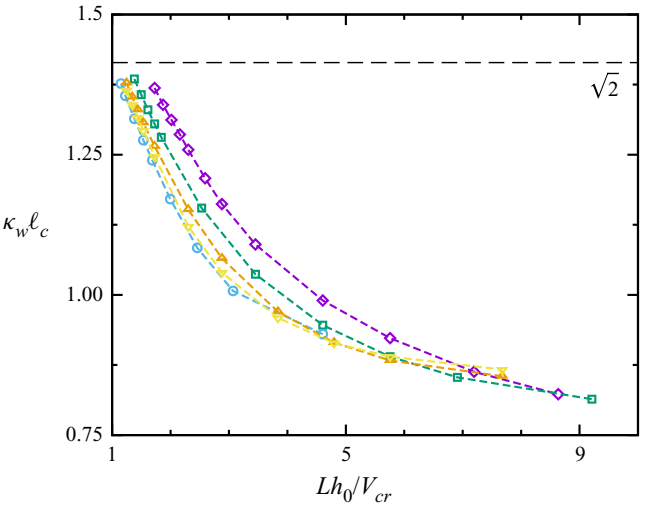

Figure 12. The maximum curvature reached by a pendant drop under a horizontal plate (i.e. the curvature corresponding to the maxima in figure 10) as a function of the normalized liquid volume Lh_0/V_{cr}. All the lines, except the second one from the left (upside down triangles, yellow) have $Ka_\perp = 21.5$. From left to right, the lines are for $L/\ell_c = 8$ (circles, blue), 10 (upside down triangles, yellow, with $Ka_\perp = 54.3$), 10 (triangles, orange), 12 (squares, green) and 15 (diamonds, purple).

vanish. A smaller g would increase the value of ℓ_c thus reducing $\kappa_\parallel$ and increasing the drop volume, for both of which ℓ_c is the characteristic length scale. The relative rapidity with which drops form as Oh is reduced may be interpreted by noting that Oh can be decreased by reducing the liquid viscosity, which permits a freer flow of liquid into the wave crest under the action of the gravity-induced pressure gradient. An equivalent interpretation may rely on reducing Oh by increasing the mean thickness of the liquid layer h_0. As can be seen from (5.1), the initial wave amplitude is given by Ah_0, and therefore a larger h_0 places a proportionately larger amount of liquid below the average liquid depth and far from the wall with a similar effect.

Figure 10 shows a monotonic increase of the maximum curvature as the crest growth is slowed down. This effect is made clearer by figure 12, which shows the maximum curvature as a function of Lh_0/V_{cr}, with $V_{cr} \simeq 5.211\ell_c^2$ Pitts' minimum volume for drop formation. Each line connects points obtained with the same values of L/ℓ_c and $Ka_\perp = 21.5$ or 54.3; the results seem to depend mostly on the total liquid volume with Ka having a minor effect. As $V/V_{cr} \to 1$, the maximum curvature increases past Pitts' κ_{cr}, although a limit value, if it exists, is not apparent from the figure. This effect is caused by a small residual amount of liquid which remains trapped on the plate near the main pendant drop. This liquid cannot readily flow into the main drop due to the strong viscous effect in the thin layer that separates it from the main drop. A similar effect was reported by Yiantsios & Higgins (1989) (see e.g. the last example in their figure 8) and, more recently, by Lister, Rallison & Rees (2010) and Lerisson *et al.* (2020). The effect is negligible when Lh_0/V_{cr} is large, but becomes noticeable when it prevents the volume ratio to get sufficiently close to 1. Because of this residual volume, the data in the figure should not really be plotted against the nominal value Lh_0/V_{cr} used in the horizontal axis of the graph, but rather against an effective volume $(Lh_0 - V_{residual})/V_{cr}$.

Figure 13(a) shows the data of figure 12 near $V/V_{cr} = 1$ which are seen to lie approximately on straight lines. We have found that the effect of the residual volume is

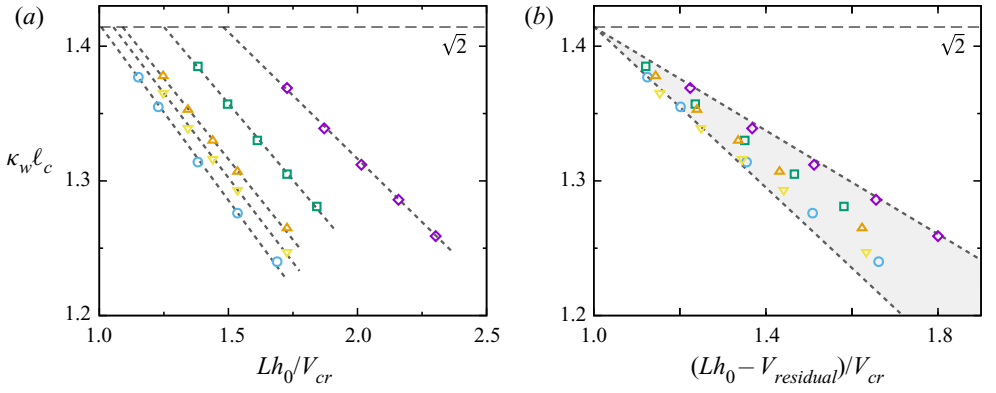

Figure 13. Panel (*a*) shows a subset of the data of figure 12 near $V/V_{cr} = 1$. Panel (*b*) shows the same data adjusted by the subtraction of $V_{residual}$ as explained in the text. See the caption to figure 12 for an explanation of the symbols.

negligible for the case with $L/\ell_c = 8$. Extrapolation of the line connecting the data for this case (open blue circles in the figure) toward $Lh_0/V_{cr} = 1$ leads to $\kappa_w \simeq \kappa_\parallel$. This fact suggests that this should be the limit for the other cases as well if the effect of the residual volume could be accounted for. In order to estimate $V_{residual}$ we extrapolate the straight lines of figure 13(*a*) to $\kappa_w = \kappa_\parallel$ and run a simulation using this initial volume with the same initial condition as before. Eventually two pendant drops are left, a larger one and a smaller one. We identify the volume of the latter with $V_{residual}$ and re-plot the data of figure 13(*a*) as functions of $(Lh_0 - V_{residual})/V_{cr}$ as shown in figure 13(*b*). All the lines now converge very closely to $\kappa_\parallel$ as $(V - V_{residual})/V_{cr} \to 1$. This procedure therefore leads to the conclusion that $\kappa_\parallel$ is indeed associated with V_{cr} when the liquid volume is just enough to cause dripping under a horizontal plate. It may be noted that the agreement with Pitts' result is not obvious *a priori* given that the present simulations were conducted under the assumption of spatial periodicity, which implies a fixed contact line at the end points of the domain, rather than fixed contact angle, conditions. A similar conclusion as to the existence of a minimum amount of liquid necessary for drop formation under conditions similar to the present ones was reached by Yiantsios & Higgins (1989) (reiterated in Kofman *et al.* 2018) and, for the three-dimensional case, by Fermigier *et al.* (1992).

The association of V_{cr} with $\kappa_\parallel$, rather than κ_{cr}, may appear somewhat unexpected. However, it is known from Pitts' work that V_{cr} is the largest liquid volume for which a drop on the underside of a horizontal plate can be stable and, as pointed out in § 4, the curvature $\kappa_\parallel$ corresponds to drop shapes for which surface tension is most effective in opposing gravity. We have seen the importance of $\kappa_\parallel$ already in figure 4 as the maximum curvature reached when drops start to form and detach, in figure 8 as being mostly close to the maximum curvature in the oscillations of Kapitza waves and in figure 10 as an upper limit for the curvature as drop formation under a horizontal plate is progressively retarded. In the first case κ_{cr} was found to play a role at the threshold, but did not appear to be associated in particular with drop formation. In the other two, the crest curvature reached and surpassed κ_{cr} without any particular feature or event marking the passage. The crucial difference between the two special values of the curvature, which explains the different importance of their roles, is that κ_{cr} is dependent on the overall wave shape and

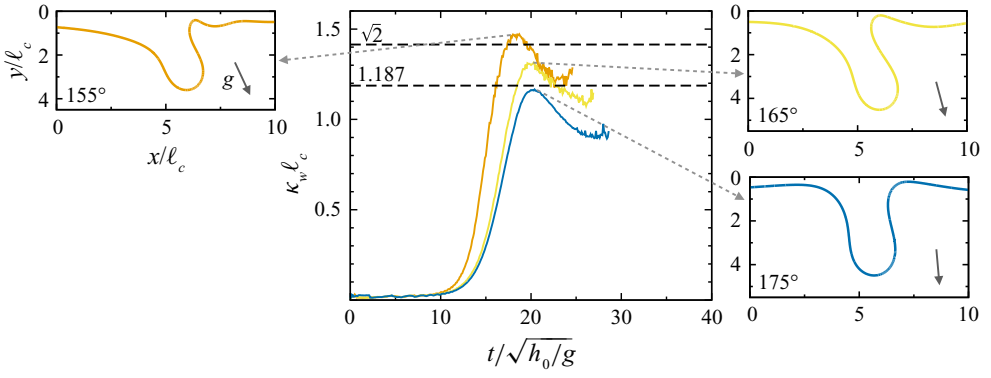

Figure 14. Continuation of figure 8 showing the curvature vs time for fixed inclination angles with $Re_\perp = 50$, $Bo_\perp = 0.6$, $V/h_0^2 = 40$. The data for $\beta = 155°$ are the same as shown in figure 8 and permit a comparison with those for $\beta = 165°$ and 175° in which cases the formation of the drop resembles that under a horizontal plate.

total liquid volume while, as already noted, the association of maximum surface-tension effect and $\kappa_\parallel$ is based only on the local features of the wave shape near the crest.

In this light, the results reported in figure 4 are not surprising: even in a flowing film, the first drops that are possible when the equilibrium provided by surface tension becomes unstable are drops with the characteristics of the (quasi-)equilibrium situation. The wave first becomes unstable when κ_{cr} is attained, but drops do not start to form and detach until the curvature reaches $\kappa_\parallel$ because it is at this point that surface tension becomes unable to support the volume of liquid in the crest. Since these are the first possible drops, one would expect that their features would be nearly independent of the total amount of liquid in the computational domain. Indeed, for example, the cases with $Re_\perp = 50$ and $Bo_\perp = 0.6$ in figure 4 go through essentially the same sequence irrespective of whether the liquid volume is $V/h_0^2 = 20$ or $V/h_0^2 = 80$. As figure 2(*b*) shows, with a larger liquid volume, drops can form at a larger plate inclination (smaller β) but the process of their formation is otherwise similar.

The residual liquid left on the plate may have a curious effect when the total liquid volume is just above V_{cr}. We have found that, in this case, the volume of the pendant drop, deprived of the residual liquid, may be below the critical value. However, the very slow motion induced by tilting the plate by as little as 1° – from 180° to 179° – is sufficient for the pendant drop to pick up the residual liquid growing sufficiently to start to drip. As pointed out by Yiantsios & Higgins (1989) and Lister *et al.* (2006), given enough time the residual volume might flow into the main drop (unless the film evaporates or breaks under the action of the disjoining pressure caused by van der Waals forces) so that it is possible that even the pendant drop on the horizontal plate might ultimately become unstable. The practical consequences of this possibility – if any – are hard to assess.

It is evident that the physics determining the evolution of the interface for a horizontal plate will not appear abruptly when the inclination angle reaches 180°, but will set in gradually as this condition is approached. For this reason, the horizontal plate results shed light on what happens when the inclination of the plate studied in § 5 is decreased to $\beta = 165°$ and 175° (figure 14). As we have already mentioned, the case with $\beta = 155°$, repeated in figure 14, is close to the critical angle and, accordingly, dripping is associated with a crest curvature close to $\kappa_\parallel$. The other two, however, are farther from the critical angle: the wave shape is markedly different, most noticeably in the tail, which is greatly diminished, and in the crest curvature, which is smaller. The amplitudes vs time of

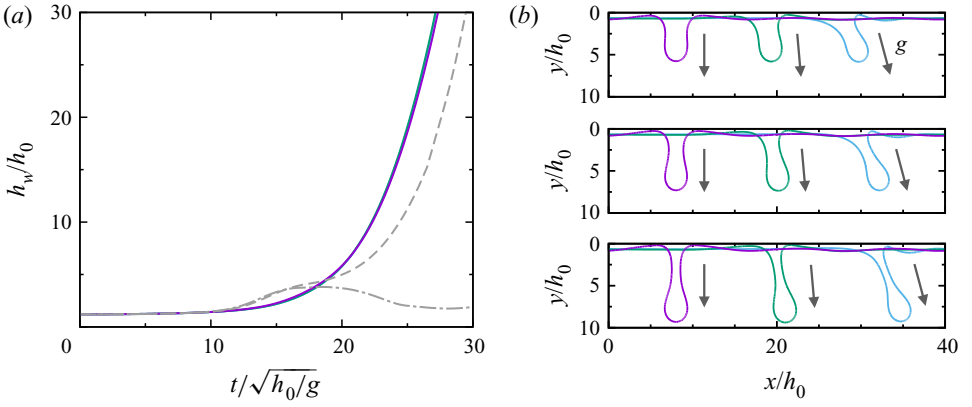

Figure 15. (*a*) Time dependence of the amplitude of the wave crests for $\beta = 180°$, 175°, 165°, 148° (all unstable) and 145° (stable). The first three very nearly superpose and are hardly distinguishable. The corresponding maximum curvatures are shown in figure 16. (*b*) Two-dimensional pendant drop shapes for the three largest inclination angles at $\sqrt{g/h_0}\,t = 20$, 21 and 22; the arrow indicates the direction of gravity. The drops slowly translate with respect to their initial position in the top panel due to the inclination of the plate.

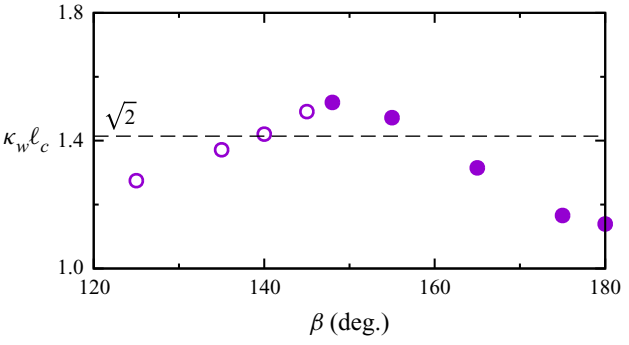

Figure 16. The maximum curvatures reached by the waves of figures 8 and 14 (augmented by the results of three additional simulations with $\beta = 180°$, $\beta = 148°$ and 140°) vs the inclination angle of the plate. The filled and open symbols denote dripping and non-dripping cases, respectively.

the waves for $\beta = 180°$, 175°, 165°, 148° (all unstable) and 145° (stable) are shown in panel (*a*) of figure 15. Remarkably, the time dependence of the first three amplitudes is virtually indistinguishable. The corresponding wave shapes, taken at the same times at three successive instants, are shown in panels (*b*) of the same figure, with the arrow indicating the direction of gravity. For these nearly horizontal plates the Rayleigh–Taylor instability develops very rapidly, much before the flow, which starts from rest, is able to generate a Kapitza wave. When the plate tilt is increased to 155° (not shown) and 148°, the growth rate weakens and finally stabilizes for an inclination of 145°.

Figure 16 collects the maximum curvatures of figures 8 and 14. The filled and open symbols denote dripping and non-dripping cases, respectively. As the dripping angle for the particular initial condition used in these simulations is approached from below, the maximum curvature of the wave increases slightly overshooting the value $\kappa_\parallel$. This is an indication that the length scale of the wave crest diminishes, a tendency which clearly favours dripping. As the angle increases past the dripping threshold, the maximum curvature decreases similarly to what we have seen for the horizontal plate case as

one moves farther away from the critical condition with increasing liquid volume and decreasing viscous effects.

7. Effect of initial conditions

A peculiarity of the present system already noted by Yiantsios & Higgins (1989), is that 'the final state of the interface can be different depending on different initial conditions and always present disturbances'. A similar point was mentioned by Rohlfs *et al.* (2017) who note that 'droplet (or ligament) detachment is sensitive to the initial condition, so that dripping ... can also occur for lower inclination numbers if a favorable initial condition is used'. Kofman *et al.* (2018) modified their original initial conditions to avoid 'a temporal development of the wave ... characterized by an overshoot in amplitude ... which accentuates the phenomenon of dripping'. While, as these quotes show, this aspect of the problem has been noted before, it does not seem to have received much attention in spite of its obvious importance. For example, it is obvious that this feature prevents the development of a phase map of possible outcomes dependent only on the problem parameters (Reynolds number etc.) such as, for example, the one developed by Rohlfs & Scheid (2015) for waves on the top side of an inclined plate. In order to be successful, any phase map must also include information on a suitable characterization of initial conditions.

The proper interpretation of these complex features must be based on concepts familiar from the theory of dynamical systems. It is well known that, when a dynamical system has more than one attractor, the phase space is divided into domains, or basins, of attraction of each one of them, with one or the other limiting behaviours ultimately prevailing depending on the particular domain of attraction in which the initial condition happens to be located (see e.g. Lichtenberg & Lieberman 1983; Wiggins 1988; Ott 2003). In a system with an infinite number of degrees of freedom like the present one, the phase space is a Sobolev space but the notion of domains of attraction still applies. There will be a domain of attraction of the dripping solution, a domain of attraction of the Kapitza wave with one hump and, possibly, domains of attraction of Kapitza waves with two or more humps, an outcome that we have occasionally encountered with long computational domains but not studied in detail. A complete characterization of these domains of attraction requires a significant effort because it must be carried out iteratively accounting for the full nonlinearity of the problem. Tools for this sort of nonlinear non-modal analysis are currently being developed (see e.g. Gallino, Schneider & Gallaire 2018; Kerswell 2018) but we will not pursue the matter here, limiting ourselves to the presentation of results of some exploratory calculations that illustrate the effect and highlight the subtlety of the influence of initial conditions.

We begin by describing the results of two types of simulations, in both of which the initial condition is given by (5.1). In the first type we start the simulations with perturbations of the same shape but different amplitudes. In the second one we use the fact that the Rayleigh–Taylor instability is dependent on the component of gravity normal to the plate, $g\cos\beta$, while the Kapitza instability is primarily dependent on the component parallel to the plate, $g\sin\beta$. If a simulation is started without the $g\cos\beta$ component, which is then restored later, the Kapitza instability is allowed to develop for a while in the absence of the other instability. This would be equivalent to imposing an initial condition on the system at the instant at which the $g\cos\beta$ component is restored.

Figure 17(*a*) shows the wave amplitude vs time when the amplitude of the initial sinusoidal perturbation (5.1) is varied from 0.1 to 0.8; the vertical Reynolds number is $Re_\perp = 50$, the Bond number $Bo_\perp = 0.6$, the liquid volume $V/h_0^2 = 40$ and the plate

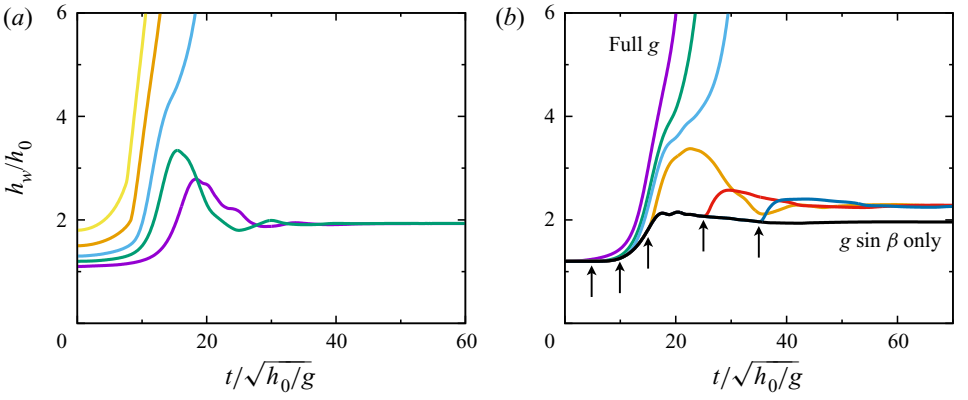

Figure 17. (*a*) Wave amplitude vs time starting from initial amplitudes $A = 0.8$, 0.5, 0.3, 0.2 and 0.1 in descending order; $Re = 50$, $Bo = 0.6$, $V/h_0^2 = 40$, $\beta = 140°$. (*b*) Wave amplitude with the gravity component normal to the plate restored at different times marked by arrows; $Re = 50$, $Bo = 0.6$, $V/h_0^2 = 40$, $\beta = 152°$. An animation of the wave growth when gravity is restored at $\sqrt{g/h_0}\,t = 10$ and $\sqrt{g/h_0}\,t = 15$ is shown in movie 2 of the supplementary material associated with this paper.

inclination angle $\beta = 140\,°$. From figure 4, the critical inclination angle for these conditions is 160.5° so that one would expect a stable non-dripping Kapitza wave in quasi-equilibrium conditions. For $A = 0.3$, 0.5 and 0.8, the vertical velocity component develops very quickly and the amplitude of the wave rapidly grows, leading to the formation and ultimate detachment of a drop. For $A = 0.1$ and 0.2, however, the wave initially grows, reaches a maximum, and then decreases settling down to a constant value. This asymptotic value is independent of the initial amplitude, showing that both initial conditions with $A = 0.1$ and 0.2 are situated in the domain of attraction of the stable steady state. Even in these stable cases, the power of the Rayleigh–Taylor instability manifests itself in causing the overshoot above the eventual steady-state level, as noted by Kofman *et al.* (2018); a similar phenomenon is responsible for the oscillation of figure 9. The smallest amplitude used here, while small, is not small enough to justify the application of linear theory. We have found that, with a truly small initial amplitude, the interface develops in a complex way with a combination of small waves with the wavelength dictated by the fastest growing Rayleigh–Taylor mode. A similar outcome is shown in figure 5 of Yiantsios & Higgins (1989).

The detaching drops in the three unstable cases of figure 17(*a*) are shown in figure 18 where it is evident that their volume increases with A. The reason is that, as anticipated in the previous section, there is a well-defined critical dripping amplitude associated with the initial condition, inclination angle and control parameters used for this simulation. Increasing A increases the distance from this critical dripping amplitude which leads to larger detaching drops. Qualitatively, this is the same tendency found for a horizontal plate in § 6 for diminishing Ohnesorge numbers. A physical interpretation is that a larger initial amplitude places more liquid into the crest of the wave at some distance from the wall from which this liquid can flow into the forming drop relatively unhindered by the viscous shear caused by the no-slip condition at the distant wall. Conversely, with a smaller initial amplitude, it takes longer for a liquid mass sufficient for dripping to collect in the wave crest as liquid flow is hindered by viscosity. Therefore, the Kapitza instability has more time to establish itself and stabilize the dripping instability by stretching the wave crest and 'opening up' the base of the drop.

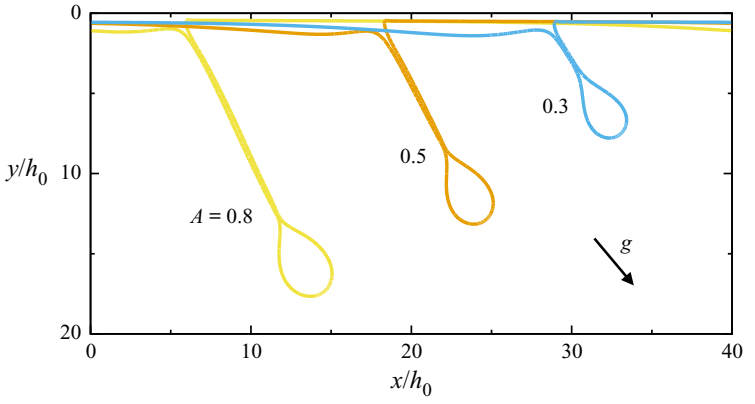

Figure 18. Drops about to detach for the three unstable cases of figure 17(*a*). From left to right the images correspond to $A = 0.8$, 0.5 and 0.3. The slight deviation of the trajectory away from the direction of gravity is due to the drag exerted by the second fluid in the computational domain as explained in § 2. Note that the structures shown here are actually two-dimensional, not real three-dimensional droplets.

Turning now to the second type of simulation, we show some results in figure 17(*b*) with the same parameter values as for the previous figure except the inclination angle that here is $\beta = 152^\circ$, again smaller than the critical angle for quasi-equilibrium conditions. The initial condition is the same sinusoid (5.1) as before with $A = 0.2$. The particular value of the inclination angle used here has been chosen because it is slightly above the stability threshold for the conditions of figure 8 and therefore, under normal conditions, it should produce an unstable wave. The curves correspond to restoring the $g\cos\beta$ gravity component at progressively later times. If the Kapitza instability is not allowed enough time to develop before the normal gravity component is restored, the wave grows and a drop eventually forms as expected. On the other hand, the film is stabilized if the action of the normal gravity component is delayed and, with it, the development of vertical inertia and the compression of the horizontal length scale toward ℓ_c. However, it is also evident from the overshoot above the eventual steady state that, as soon as it is restored, the Rayleigh–Taylor instability injects a significant amount of energy into the system 'trying' to destabilize the wave. In this case as well the amplitude of the steady-state wave is independent of the time at which the vertical gravity component is restored and the same comment on the location of the initial conditions in the domains of attractions of the two asymptotic solutions is applicable. An animation of the wave growth when gravity is restored at $\sqrt{g/h_0}\,t = 10$ and $\sqrt{g/h_0}\,t = 15$ is shown in movie 2 of the supplementary material associated with this paper.

In both previous cases the initial condition was a sinusoid with a wavelength equal to that of the computational domain. We now show results obtained with different initial shapes. For the first example we use

$$\frac{h(x,\,t=0)}{h_0} = 1 + \frac{A}{\tau}\tan^{-1}\frac{\tau\sin 2\pi x/L}{1-\tau\cos 2\pi x/L}, \tag{7.1}$$

with $0 \le \tau \le 1$ a dimensionless parameter. The shape of this curve which, depending on τ, interpolates between a single sine ($\tau = 0$) and a sawtooth function ($\tau = 1$) (McCaughan 2017), is shown in figure 19 for $\tau = 0.5$ and $A = -0.3$ (forward leaning, solid line) and $A = 0.3$ (backward leaning, dashed line). Figure 20, for $Re_\perp = 50$, $Bo_\perp = 0.6$ and $V/h_0^2 = 40$, shows that a significant difference between the two cases

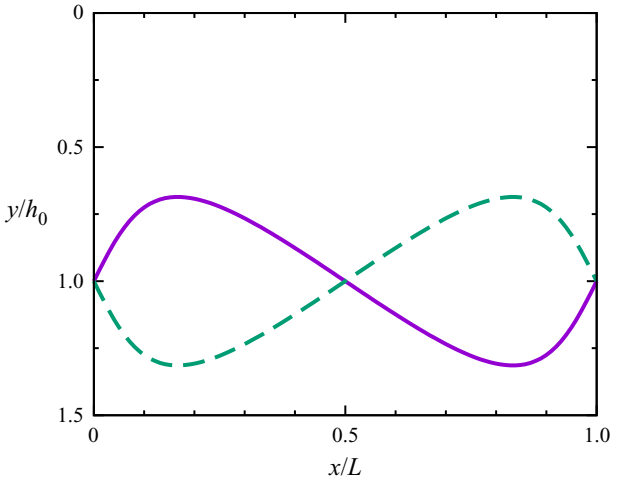

Figure 19. The initial condition (7.1) for a 'forward-leaning sine' ($A = -0.3$, solid line) and a backward-leaning sine ($A = 0.3$, dashed line) with $\tau = 0.5$; note the downward-oriented vertical axis.

develops already for $A = \pm 0.1$, with the forward-leaning wave becoming stable and the backward-leaning one unstable. A close inspection shows that the oscillations affecting the forward-leaning case with $A = -0.1$ are not due to the Fourier modes that make up the initial condition, but to small capillary disturbances absorbed at the front of the wave as for the oscillations of figure 8. Thus, a Fourier decomposition is of little value in determining the dripping/non-dripping outcome of the wave development. The same difference between forward- and backward-leaning initial shapes persists all the way to $A = \pm 0.4$ while, for $A = \pm 0.5$, both initial shapes become unstable. A likely explanation of the different outcomes is that, in the forward-leaning case, the initial shape is already close to that of a Kapitza wave and such that surface tension starts out strong (cf. a similar argument in Babchin *et al.* 1983), while its effect has to gradually develop in the backward-leaning case leaving enough time for the liquid to accumulate into the wave crest and ultimately drip.

As a fourth example we use the superposition of two sines

$$\frac{h(x, t = 0)}{h_0} = 1 + A\left(\sin\frac{2\pi x}{L} + 0.1\sin\frac{4\pi x}{L}\right). \tag{7.2}$$

The maximum and minimum amplitudes of this shape differ by less than 2 % from $\pm A$ and, therefore, these simulations can legitimately be compared with the results found omitting the second term (dashed lines). Both initial conditions produce stable Kapitza waves for $A = 0.1$ and unstable waves for $A = 0.3$ and 0.5. However, for $A = 0.2$, the one-term initial condition produces a stable wave while the two-term one produces an unstable solution. These results illustrate the sharpness and convoluted shape of the domains of attraction of the two asymptotic solutions, demonstrating the difficulties that must be overcome to understand their topologies and, even more, to develop a precise determination of their boundaries. It is also interesting to note that the solid lines give no straightforward evidence of the presence of two Fourier components in the initial condition. The nonlinear interaction is evidently quite strong already from the beginning.

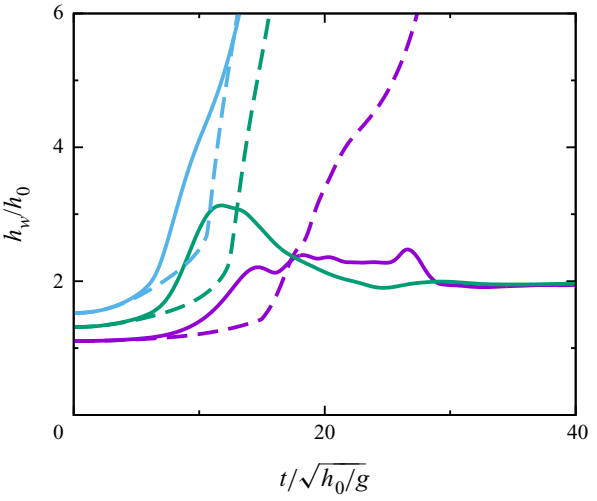

Figure 20. Evolution of h_w/h_0, the normalized maximum height of the wave, for the initial conditions (7.1) with $\tau = 0.5$. The solid lines are for a forward tilt and the dashed lines for a backward tilt. In descending order, the lines are for $A = \pm 0.5$ (blue), ± 0.3 (green) and ± 0.1 (purple).

8. Summary and conclusions

In this paper we have considered the dripping of a liquid film flowing along the underside of a titled plate. The Rayleigh–Taylor instability tends to cause dripping by reducing the length scale of the wave crest so much that the weight of the liquid that concentrates into it cannot be sustained by surface tension. Conversely, the Kapitza wave owes its stabilizing effect to its ability to prevent the accumulation of liquid in the crest by thickening the wave tail and stretching its length scale. We have found that, when the wave is allowed to evolve in quasi-equilibrium conditions, the balance of gravity and surface tension is broken in much the same way as when a drop forms on the underside of a horizontal plate when the liquid is just sufficient for this to happen (Pitts 1973). Key to the establishment of this correspondence has been our recasting of Pitts' stability condition in terms of the curvature of the wave crest, which does not rely on the contact angles and liquid volumes used in his original formulation. In this way, the crest curvature has been turned into a sensitive indicator of the liquid volume in the crest and of the proximity of the crest to the dripping instability. As dynamic effects become important, the value of the crest curvature as an indicator of the weight of the liquid accumulated in it weakens, but remains fairly good provided conditions are not too far from the quasi-equilibrium dripping threshold. Increasing distance from the threshold, as in the case of a horizontal or nearly horizontal plate or a large-amplitude initial condition, produces progressively larger drops with decreasing maximum curvature.

The dependence of the outcome of the simulations on initial conditions, which has been noted, but not studied in depth, before (Yiantsios & Higgins 1989; Rohlfs *et al.* 2017; Kofman *et al.* 2018), is a very striking feature of the process investigated in this work. The analysis of the horizontal plate case reveals an important factor that suggests an explanation for this effect, namely the need for the rapid flow of liquid into the wave crest. If the initial condition places enough liquid relatively far from the supporting plate, this liquid can rapidly flow into the crest because it is relatively unhindered by the viscous shear caused by the no-slip condition at the plate. In this case, then, a drop is more likely to form. By 'stretching' the wave, the flow pushes the liquid closer to the plate thus subjecting

it to viscous shear and preventing it from flowing into the crest to form a drop. For this stabilizing process to take place, though, enough time must be allowed for the Kapitza wave to develop which, depending on conditions, may be too long to stop the dripping instability. In support of this explanation we have shown that, if the Kapitza instability is allowed sufficient time to establish itself before the Rayleigh–Taylor instability is turned on, dripping is prevented. As the flow Reynolds number is increased, the tail behind the crest of the wave becomes longer and thicker and, therefore, by conservation of mass, the wave amplitude decreases, both effects countering the development of a large curvature. Indeed, we have found that smaller Reynolds numbers are less stable than larger ones.

With the domain lengths on which we have focused (up to 80 times as long as the mean film thickness) and with the initial conditions that we have considered, we have not found a tendency for the appearance of a second wave and, therefore, we have not had to deal with wave–wave interactions. There are several reasons why these interactions are important for film flow above a plate (see e.g. Chang & Demekhin 2002; Pradas, Tseluiko & Kalliadasis 2011; Pradas, Kalliadasis & Tseluiko 2012). An additional one for a film on the underside of a plate is that, as shown experimentally by Fermigier *et al.* (1992), dripping can result from the coalescence of two waves which, individually, would be stable. Another important class of problems related to the one we have investigated is film flow on the underside of curved, rather than planar, surfaces which is important, for instance, for vapor condensation on tubes in heat exchangers and other applications (see e.g. Limat *et al.* 1992; Takagi & Huppert 2010; Balestra, Nguyen & Gallaire 2018). It may be expected that our focus on the crest curvature as an indicator of the formation of short length scales conducive to dripping as well as the quasi-equilibrium approximation would be relevant for such applications as well.

In conclusion it is appropriate to consider which of our findings would likely carry over to the three-dimensional situation. The quasi-equilibrium result of § 4 is only based on the fact that the balance of surface tension and gravity that governs dripping from a horizontal plate is also relevant in the case of waves on a flowing film provided the limit angle is approached very slowly. It would seem that this conclusion should apply to the three-dimensional problem as well. The marked effect of initial conditions is a qualitative feature that should be strong enough to carry over to the three-dimensional case. The mechanism leading to oscillations such as those shown in figures 8, 9 and 14 should affect also a three-dimensional process. No such oscillations have yet been observed in experiments, but this could be due to small Reynolds numbers, large viscosity, small surface tension or a combination of these factors. For example, in the experiments of Brun *et al.* (2015) $Re \leq 0.1$, in those of Rietz *et al.* (2017), $Re \leq 1.6$; in those of Charogiannis *et al.* (2018) $Re \leq 193$, but the smallest Kapitza number was 13.1; in those of Ledda *et al.* (2020) the Kapitza number was approximately 0.087. The role of the substrate and wave tail in 'stretching' the wave crest, limiting the curvature and thereby stabilizing the wave appears to be a robust qualitative feature which may also be expected to affect the three-dimensional flow.

Supplementary movies. Supplementary movies are available at https://doi.org/10.1017/jfm.2021.1032.

Funding. This study was supported by the University of Houston. The numerical computations were carried out on the Sabine cluster of the University of Houston Research Computing Data Core.

Declaration of interests. The authors report no conflict of interest.

Author ORCIDs.
Guangzhao Zhou https://orcid.org/0000-0002-9721-9628;
Andrea Prosperetti https://orcid.org/0000-0003-4129-7130.

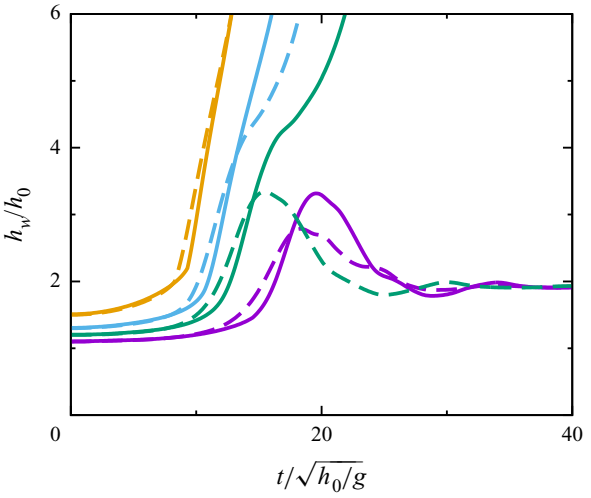

Figure 21. Wave evolution from the two-term initial condition (7.2) with (solid lines) and without (dashed lines) the second Fourier component; $A = 0.1$ (purple), $A = 0.2$ (green), $A = 0.3$ (blue) and $A = 0.5$ (orange).

Appendix A. Drop under a horizontal plate

Explicitly, the surface-tension–gravity balance (4.1) is

$$\frac{\ell_c^2 z''}{(1+z'^2)^{3/2}} = \ell_c^2 \kappa_0 - z, \tag{A1}$$

with primes denoting differentiation with respect to the variable x and κ_0 the tip curvature. The x coordinate runs parallel to the plate and the z coordinate is vertical directed toward the plate with the origin at the drop tip. For the problem of a pendant drop under a horizontal plate the solution is required to satisfy the condition $z' = 0$ at $x = 0$ and a prescribed contact angle on the plate, which is zero in the situation of present interest. The problem can be solved exactly (see e.g. Pitts 1973; Tanasijczuk, Perazzo & Gratton 2010; Lerisson *et al.* 2020). Here, we focus on some aspects of direct relevance to the considerations of § 4.

At the inflection point (index ip) $z'' = 0$ and, therefore,

$$z_{ip} = \kappa_0 \ell_c^2. \tag{A2}$$

The transformation $\tilde{z} = 2z_{ip} - z, \tilde{x} = 2x_{ip} - x$ leaves the equation unchanged transforming the condition $z' = 0$ at the tip ($x = 0$, $z = 0$) into the condition $\mathrm{d}\tilde{z}/\mathrm{d}\tilde{x} = 0$ at ($\tilde{x} = 2x_{ip}$, $\tilde{z} = 2z_{ip}$) and the condition $z' = 0$ at ($x = 2x_{ip}$, $z = 2z_{ip}$) into the condition $\mathrm{d}\tilde{z}/\mathrm{d}\tilde{x} = 0$ at ($\tilde{x} = 0$, $\tilde{z} = 0$). It also follows that $z''(0) = -\mathrm{d}^2\tilde{z}/\mathrm{d}\tilde{x}^2|_{\tilde{x}=0}$ so that the curvatures at the tip and at the base are opposite and (4.2) directly follows from (4.1). The previous argument also shows that the total height of the pendant drop is $2z_{ip}$ and that its shape is symmetric about (x_{ip}, z_{ip}). It is therefore evident that the volume of the pendant drop (per unit spanwise length) is given by

$$V = (2z_{ip}) \times (2x_{ip}). \tag{A3}$$

In order to determine x_{ip} we need to integrate (A1) from $z = 0$ to $z = z_{ip}$. For this purpose we make a change of the independent variable from x to z setting $z' = p(z)$.

With this step, which is legitimate as long as the relation $z(x)$ is one-to-one, the equation can be integrated once from $z = 0$, where $p = 0$, to find

$$-\frac{2\ell_c^2}{\sqrt{1+p^2}} + 2\ell_c^2 = 2\ell_c^2\kappa_0 z - z^2. \tag{A4}$$

With the definitions

$$Z = 1 - \frac{z}{z_{ip}}, \quad X = \frac{x}{z_{ip}}, \quad H = \frac{2\ell_c^2}{z_{ip}^2} = \frac{2}{\ell_c^2\kappa_0^2}, \tag{A5a–c}$$

(A4) becomes

$$\frac{\mathrm{d}Z}{\mathrm{d}X} = -\frac{\sqrt{(1-Z^2)(Z^2+2H-1)}}{Z^2+H-1}. \tag{A6}$$

Separating variables and integrating from $(X = 0,\ Z = 1)$ to $(X = X_{ip},\ Z = 0)$ we can write

$$X_{ip} = \frac{1}{k}\int_0^1 \sqrt{\frac{1-k^2(1-Z^2)}{1-Z^2}}\,\mathrm{d}Z - \frac{1}{2k}\int_0^1 \frac{\mathrm{d}Z}{\sqrt{(1-Z^2)[1-k^2(1-Z^2)]}}, \tag{A7}$$

in which $k = 1/\sqrt{2H}$. The integrals can be reduced to complete elliptic integrals of the second and first kinds, respectively, so that the result of the integration is

$$X_{ip} = \frac{\boldsymbol{E}(k)}{k} - \frac{\boldsymbol{K}(k)}{2k}. \tag{A8}$$

The volume (A3) is then given by

$$\frac{V}{\ell_c^2} = 8\ell_c\kappa_0\left(\boldsymbol{E}(k) - \frac{1}{2}\boldsymbol{K}(k)\right) = 16k\left(\boldsymbol{E}(k) - \frac{1}{2}\boldsymbol{K}(k)\right). \tag{A9}$$

The liquid volume for the special shape with vertical tangents at the inflection points can be found by noting that, at that point, $p = 0$ in (A4) so that $\kappa_0 = \sqrt{2}/\ell_c$ and the modulus of the elliptic integral becomes $k = 1/\sqrt{2}$. For this special value $\boldsymbol{E} - \boldsymbol{K}/2 = (\pi/\boldsymbol{K})/4$ and $\boldsymbol{K}(1/\sqrt{2}) = (4\sqrt{\pi})^{-1}[\Gamma(1/4)]^2$ with Γ the Gamma function. Thus we find

$$\frac{V_\parallel}{\ell_c^2} = \frac{16\pi^{3/2}}{\sqrt{2}\Gamma^2(1/4)} \simeq 4.793. \tag{A10}$$

It is also interesting to note that, in this case, the volume V_M of the part of the drop under the points with vertical tangent can be simply found from the balance $\rho g V_M = 2\sigma$ from which $V_M = 2\ell_c^2$. In this case $z_{ip} = \sqrt{2}\ell_c$ and the height of the horizontal plate above the tip of the drop is $2\sqrt{2}\ell_c$.

Appendix B. The scaling of Kofman *et al.* (2018)

In Kofman *et al.* (2018) the authors propose scaling relations for the four forces (per unit spanwise length) assumed to determine the dripping at onset, namely surface tension F_σ,

Critical angle	$Re_\perp \sin\beta$	$Ka_\perp$	F_σ	F_g	F_v	F_m	$\sum F_i$
171°	7.82	70.6	28	−70	4	41	3
165°	12.9	70.6	33	−58	7	133	116
168°	20.8	112	49	−100	9	254	211
164°	13.8	70.6	34	−57	8	154	139
161°	16.3	47.1	27	−46	9	260	251
158°	18.7	35.3	24	−39	11	398	393

Table 1. The estimates (B1) to (B4) of the forces and their sum applied to the cases of figure 4, from left to right, at threshold.

gravity F_g , viscosity F_v and inertia F_m. In our notation, these relations are

$$\frac{F_\sigma}{\rho g^{1/3}\nu^{4/3}} \sim \left(\frac{3Re_\perp}{Bo_\perp}\right)^{2/3} (\sin\beta)^{1/3}, \tag{B1}$$

$$\frac{F_g}{\rho g^{1/3}\nu^{4/3}} \sim \left(\frac{9Re_\perp^2}{Bo_\perp}\right)^{1/3} \frac{\cos\beta}{(\sin\beta)^{1/3}}, \tag{B2}$$

$$\frac{F_v}{\rho g^{1/3}\nu^{4/3}} \sim (3Re_\perp)^{2/3} \sin\beta, \tag{B3}$$

$$\frac{F_m}{\rho g^{1/3}\nu^{4/3}} \sim (3Re_\perp)^{5/3}\, Bo_\perp^{1/3} (\sin\beta)^{7/3}. \tag{B4}$$

Dripping is avoided as long as these forces are in approximate balance. It is interesting to apply these estimates to the cases of figure 4 at threshold. The results are shown in table 1. It would appear that the momentum term F_m is systematically over-estimated except, perhaps, in the first case. This is peculiar as the threshold angles calculated by the method of figure 4 correspond to quasi-equilibrium conditions in which momentum effects would be expected to be small.

References

Abdelall, F.F., Abdel-Khalik, S.I., Sadowski, D.L., Shin, A. & Yoda, M. 2006 On the Rayleigh–Taylor instability for confined liquid films with injection through the bounding surfaces. *Intl J. Heat Mass Transfer* **49**, 1529–1546.

Alekseenko, S.V., Nakoryakov, V.E. & Pokusaev, B.G. 1994 *Wave Flow of Liquid Films*. Begell House.

Babchin, A.J., Frenkel, A.L., Levich, B.G. & Sivashinsky, G.I. 1983 Nonlinear saturation of Rayleigh–Taylor instability in thin films. *Phys. Fluids* **26**, 3159–3161.

Balestra, G., Nguyen, D.M.-P. & Gallaire, F. 2018 Rayleigh–Taylor instability under a spherical substrate. *Phys. Rev. Fluids* **3**, 084005.

Bertagni, M.B. & Camporeale, C. 2017 Nonlinear and subharmonic stability analysis in film-driven morphological patterns. *Phys. Rev.* E **96**, 053115.

Brackbill, J.U., Kothe, D.B. & Zemach, C. 1992 A continuum method for modeling surface tension. *J. Comput. Phys.* **100**, 335–354.

Brun, P.-T., Damiano, A., Pierre, R., Balestra, G. & Gallaire, F. 2015 Rayleigh–Taylor instability under an inclined plane. *Phys. Fluids* **27**, 084107.

Chang, H.-C. 1994 Wave evolution on a falling film. *Annu. Rev. Fluid Mech.* **26**, 103–136.

Chang, H.-C. & Demekhin, E.A. 2002 *Complex Wave Dynamics on Thin Films*. Elsevier.

CHAROGIANNIS, A., DENNER, F., VAN WACHEM, B.G.M., KALLIADASIS, S., SCHEID, B. & MARKIDES, C.N. 2018 Experimental investigations of liquid falling films flowing under an inclined planar substrate. *Phys. Rev. Fluids* **3**, 114002.

CRASTER, R.V. & MATAR, O.K. 2009 Dynamics and stability of thin liquid films. *Rev. Mod. Phys.* **81**, 1131–1198.

DEISSLER, R.J. & ORON, A. 1992 Stable localized patterns in thin liquid films. *Phys. Rev. Lett.* **68**, 2948–2951.

DENNER, F., CHAROGIANNIS, A., PRADAS, M., MARKIDES, C.N., VAN WACHEM, B.G.M. & KALLIADASIS, S. 2018 Solitary waves on falling liquid films in the inertia-dominated regime. *J. Fluid Mech.* **837**, 491–519.

DIETZE, G.F. 2019 Effect of wall corrugations on scalar transfer to a wavy falling liquid film. *J. Fluid Mech.* **859**, 1098–1128.

DUPRAT, C., RUYER-QUIL, C., KALLIADASIS, S. & GIORGIUTTI-DAUPHINÉ, F. 2007 Absolute and convective instabilities of a film flowing down a vertical fiber. *Phys. Rev. Lett.* **98**, 244502.

ELGOWAINY, A. & ASHGRIZ, N. 1997 The Rayleigh–Taylor instability of viscous fluid layers. *Phys. Fluids* **9**, 1635–1649.

FERMIGIER, M., LIMAT, L., WESFREID, J.E., BOUDINET, P. & QUILLIET, C. 1992 Two-dimensional patterns in Rayleigh–Taylor instability of a thin layer. *J. Fluid Mech.* **236**, 349–383.

FRANÇOIS, M.M., CUMMINS, S.J., DENDY, E.D., KOTHE, D.B., SICILIAN, J.M. & WILLIAMS, M.W. 2006 A balanced-force algorithm for continuous and sharp interfacial surface tension models within a volume tracking framework. *J. Comput. Phys.* **213**, 141–173.

GALLINO, G., SCHNEIDER, T.M. & GALLAIRE, F. 2018 Edge states control droplet breakup in subcritical extensional flows. *Phys. Rev. Fluids* **3**, 073603.

INDEIKINA, A., VERETENNIKOV, I. & CHANG, H.-C. 1997 Drop fall-off from pendent rivulets. *J. Fluid Mech.* **338**, 173–201.

KALLIADASIS, S. & CHANG, H.-C. 1994 Drop formation during coating of vertical fibres. *J. Fluid Mech.* **261**, 135–168.

KALLIADASIS, S., RUYER-QUIL, C., SCHEID, B. & VELARDE, M.G. 2011 *Falling Liquid Films*. Springer.

KAPITZA, P.L. 1948 Wave flow of thin layers of a viscous fluid. I. The free flow. *Zh. Eksp. Teor. Fiz.* **18**, 3, English translation available in *Collected Papers of P. L. Kapitza* (ed. D. ter Haar), vol. 2, pp. 663–679, Pergamon, 1965.

KAPITZA, P.L. & KAPITZA, S.P. 1949 Wave flow of thin layers of viscous liquids. III. Experimental study of undulatory flow conditions. *Zh. Eksp. Teor. Fiz.* **19**, 105, English translation available in *Collected Papers of P. L. Kapitza* (ed. D. ter Haar), vol. 2, pp. 690–709, Pergamon, 1965.

KERSWELL, R.R. 2018 Nonlinear nonmodal stability theory. *Annu. Rev. Fluid Mech.* **50**, 319–345.

KOFMAN, N., ROHLFS, W., GALLAIRE, F., SCHEID, B. & RUYER-QUIL, C. 2018 Prediction of two-dimensional dripping onset of a liquid film under an inclined plane. *Intl J. Multiphase Flow* **104**, 286–293.

KONDIC, L. 2003 Instabilities in gravity driven flow of thin fluid films. *SIAM Rev.* **95**, 45–115.

LEDDA, P.G., BALESTRA, G., LERISSON, G., SCHEID, B., WYART, M. & GALLAIRE, F. 2021 Hydrodynamic-driven morphogenesis of karst draperies: spatio-temporal analysis of the two-dimensional impulse response. *J. Fluid Mech.* **910**, A53.

LEDDA, P.G., LERISSON, G., BALESTRA, G. & GALLAIRE, F. 2020 Instability of a thin viscous film flowing under an inclined substrate: the emergence and stability of rivulets. *J. Fluid Mech.* **904**, A23.

LERISSON, G., LEDDA, P.G., BALESTRA, G. & GALLAIRE, F. 2020 Instability of a thin viscous film flowing under an inclined substrate: steady patterns. *J. Fluid Mech.* **898**, A6.

LICHTENBERG, A.J. & LIEBERMAN, M.A. 1983 *Regular and Stochastic Motion*. Springer.

LIMAT, L., JENFFER, P., DAGENS, B., TOURON, E., FERMIGIER, M. & WESFREID, J.E. 1992 Gravitational instabilities of thin liquid layers: dynamics of pattern selection. *Physica* D **61**, 166–182.

LIN, T.-S. & KONDIC, L. 2010 Thin films flowing down inverted substrates: two dimensional flow. *Phys. Fluids* **22**, 052105.

LIN, T.-S., KONDIC, L. & FILIPPOV, A. 2012 Thin films flowing down inverted substrates: three-dimensional flow. *Phys. Fluids* **24**, 022105.

LISTER, J.R. & KERR, R.C. 1989 The effect of geometry on the gravitational instability of a buoyant region of viscous fluid. *J. Fluid Mech.* **202**, 577–594.

LISTER, J.R., RALLISON, J.M., KING, A.A., CUMMINGS, L.J. & JENSEN, O.E. 2006 Capillary drainage of an annular film: the dynamics of collars and lobes. *J. Fluid Mech.* **552**, 311–343.

LISTER, J.R., RALLISON, J.M. & REES, S.J. 2010 The nonlinear dynamics of pendent drops on a thin film coating the underside of a ceiling. *J. Fluid Mech.* **647**, 239–264.

McCaughan, G. 2017 Equation of a 'tilted' sine, https://math.stackexchange.com/questions/2430564/equation-of-a-tilted-sine/2430837#2430837, accessed May 31, 2021.
Oron, A., Davis, S.H. & Bankoff, S.G. 1997 Long-scale evolution of thin liquid films. *Rev. Mod. Phys.* **69**, 931–980.
Orsini, G. & Tricoli, V. 2017 A scaling theory of the free-coating flow on a plate withdrawn from a pool. *Phys. Fluids* **29**, 052106.
Ott, E. 2003 *Chaos in Dynamical Systems*, 2nd edn. Cambridge University Press.
Pitts, E. 1973 The stability of pendent liquid drops. Part 1. Drops formed in a narrow gap. *J. Fluid Mech.* **59**, 753–767.
Popinet, S. 2009 An accurate adaptive solver for surface-tension-driven interfacial flows. *J. Comput. Phys.* **228**, 5838–5866.
Pradas, M., Kalliadasis, S. & Tseluiko, D. 2012 Binary interactions of solitary pulses in falling liquid films. *IMA J. Appl. Maths* **77**, 408–419.
Pradas, M., Tseluiko, D. & Kalliadasis, S. 2011 Rigorous coherent-structure theory for falling liquid films: viscous dispersion effects on bound-state formation and self-organization. *Phys. Fluids* **23**, 044104.
Pumir, A., Manneville, T. & Pomeau, Y. 1983 On solitary waves running down an inclined plane. *J. Fluid Mech.* **135**, 27–50.
Reck, D. & Aksel, N. 2015 Recirculation areas underneath solitary waves on gravity-driven film flows. *Phys. Fluids* **27**, 112107.
Rietz, M., Scheid, B., Gallaire, F., Kofman, N., Kneer, R. & Rohlfs, W. 2017 Dynamics of falling films on the outside of a vertical rotating cylinder: waves, rivulets and dripping transitions. *J. Fluid Mech.* **832**, 189–211.
Rohlfs, W., Pischke, P. & Scheid, B. 2017 Hydrodynamic waves in films flowing under an inclined plane. *Phys. Rev. Fluids* **2**, 044003.
Rohlfs, W. & Scheid, B. 2015 Phase diagram for the onset of circulating waves and flow reversal in inclined falling films. *J. Fluid Mech.* **763**, 322–351.
Ruyer-Quil, C. & Manneville, P. 2000 Improved modeling of flows down inclined planes. *Eur. Phys. J.* **B15**, 357–369.
Scardovelli, R. & Zaleski, S. 1999 Direct numerical simulation of free-surface and interfacial flow. *Annu. Rev. Fluid Mech.* **31**, 567–603.
Scheid, B., Kofman, N. & Rohlfs, W. 2016 Critical inclination for absolute/convective instability transition in inverted falling films. *Phys. Fluids* **28**, 044107.
Sterman-Cohen, E., Bestehorn, M. & Oron, A. 2017 Rayleigh–Taylor instability in thin liquid films subjected to harmonic vibration. *Phys. Fluids* **29**, 052105, erratum: *Phys. Fluids*, vol. 29, 109901.
Sterman-Cohen, E. & Oron, A. 2020 Dynamics of nonisothermal two-thin-fluid-layer systems subjected to harmonic tangential forcing under Rayleigh–Taylor instability conditions. *Phys. Fluids* **32**, 082113.
Takagi, D. & Huppert, H.E. 2010 Flow and instability of thin films on a cylinder and sphere. *J. Fluid Mech.* **647**, 221–238.
Talib, E. & Juel, A. 2007 Instability of a viscous interface under horizontal oscillation. *Phys. Fluids* **19**, 092102.
Tanasijczuk, A.J., Perazzo, C.A. & Gratton, J. 2010 Navier–Stokes solutions for steady parallel-sided pendent rivulets. *Eur. J. Mech. B/Fluids* **29**, 465–471.
Tomlin, R.J., Cimpeanu, R. & Papageorgiou, D.T. 2020 Instability and dripping of electrified liquid films flowing down inverted substrates. *Phys. Rev. Fluids* **5**, 013703.
Trinh, P., Kim, H., Hammoud, N., Howell, P., Chapman, S. & Stone, H. 2014 Curvature suppresses the Rayleigh–Taylor instability. *Phys. Fluids* **26**, 051704.
Weinstein, S.J. & Ruschak, K.J. 2004 Coating flows. *Annu. Rev. Fluid Mech.* **36**, 29–53.
Whitehead, J.A. 1988 Fluid models of geological hot spots. *Annu. Rev. Fluid Mech.* **20**, 61–87.
Wiggins, S. 1988 *Global Bifurcations and Chaos*. Springer.
Wolf, G.H. 1969 The dynamic stabilization of the Rayleigh–Taylor instability and the corresponding dynamic equilibrium. *Z. Phys.* **227**, 291–300.
Yiantsios, S.G. & Higgins, B.G. 1989 Rayleigh–Taylor instability in thin viscous films. *Phys. Fluids* **A1**, 1484–1501.
Zhou, G. & Prosperetti, A. 2020 Capillary waves on a falling film. *Phys. Rev. Fluids* **5**, 114005.